RESEARCH ARTICLE

Key Points:

- Magnetosheath reconnection is driven by interaction of the interplanetary rotational discontinuity (RD) with the bow shock/magnetosheath
- The existent and structure of reconnection depending on the solar wind Alfvén Mach number and the propagation direction of the RD
- Large-amplitude low-frequency waves downstream of the Q-∥ shock play an important role in triggering reconnection inside the RD

Correspondence to:

Z. Guo,
guozf@mail.iggcas.ac.cn

Global Hybrid Simulations of Interaction Between Interplanetary Rotational Discontinuity and Bow Shock/Magnetosphere: Can Ion-Scale Magnetic Reconnection be Driven by Rotational Discontinuity Downstream of Quasi-Parallel Shock?

Zhifang Guo[1] ![ORCID], **Yu Lin[1]** ![ORCID], **and Xueyi Wang[1]** ![ORCID]

[1]Department of Physics, Auburn University, Auburn, AL, USA

Abstract Ion-scale magnetic reconnection has been observed downstream of the terrestrial quasi-parallel (Q-∥) shock. Whether it is driven by interplanetary discontinuities or turbulent Q-∥ shock, however, is unclear. Using three-dimensional global hybrid simulation, we investigate the generation of magnetic reconnection downstream of the Q-∥ shock, while an interplanetary rotational discontinuity (RD) is launched to the bow shock. Cases with various solar wind Alfvén Mach numbers, $M_A = 3.0$ to 8, and propagation directions of the RD are presented. The propagation direction n is assumed to be in the GSE xz plane and pointing earthward, with $n = (-\sin(\theta_{12}/2), 0, -\cos(\theta_{12}/2))$, where θ_{12} is the angle between the upstream (B_1) and downstream (B_2) magnetic fields across the transmitted RD. It is found that magnetic reconnection occurs inside the RD downstream of the Q-∥ shock, forming flux ropes extending along the dawn-dusk direction about tens of ion inertial lengths. Large-amplitude low-frequency waves originated from the Q-∥ shock lead to the bending and squeezing of the field lines around the RD, which play an important role in triggering reconnection inside the RD. As the RD impacts the dayside magnetopause, magnetopause reconnection takes place between the field lines behind the RD and geomagnetic field lines. Nevertheless, no reconnection is found downstream of the Q-∥ shock itself or outside the RD in the magnetosheath. The existent and structure of reconnection in the magnetosheath are found to strongly depend on the parameters M_A and n. Our simulation shows that ion-scale magnetic reconnection is driven by an external driver in the form of the compression of an RD around the bow shock and in the magnetosheath, rather than caused by the turbulent Q-∥ shock alone.

1. Introduction

Current sheets in the solar wind can exist where there are magnetohydrodynamic (MHD) discontinuities, as observed since early spacecraft measurements of the interplanetary magnetic field (IMF) (e.g., Behannon et al., 1981; Burlaga et al., 1969; Horbury et al., 2001; Lepping & Behannon, 1986; Tsurutani & Smith, 1979). These frequently observed events are usually described by either rotational discontinuities (RDs) or tangential discontinuities (TDs). Among them, TDs can be considered as magnetic boundary layers without the normal component of magnetic field ($B_n = 0$), with a total pressure balance. TDs convect with the solar wind flows. On the other hand, RDs can be considered as large-amplitude Alfvén waves with a finite normal magnetic field, that is, $B_n \neq 0$. RDs propagate with the normal Alfvén speed V_{An} relative to the background plasma.

Interaction of an interplanetary RD with the Earth's bow shock has been investigated for decades (e.g., Archer et al., 2012; Cable & Lin, 1998; Karlsson et al., 2018; Lin, 1997; Lin, Lee, et al., 1996; Lin, Swift, et al., 1996; Sibeck et al., 1997; Tsubouchi & Matsumoto, 2005; Yan & Lee, 1994, 1996). Using one-dimensional (1D) and two-dimensional (2D) MHD simulations, Yan and Lee (1994, 1996) suggested that the interaction between an RD and the bow shock results in a pair of slow shocks and an intermediate shock. The MHD simulation of Sibeck et al. (1997) predicted that both slow mode waves and sunward-/antisunward-moving Alfvén waves are generated in the magnetosheath after the bow shock/RD interaction. The interaction of interplanetary RDs with the bow shock may also cause the generation of pressure pulses in the magnetosheath,

as suggested by simulations (Cable & Lin, 1998; Lin, Lee, et al., 1996; Lin, Swift, et al., 1996; Tsubouchi & Matsumoto, 2005) and observations (Archer et al., 2012; Karlsson et al., 2018).

Magnetic reconnection has been observed in the magnetosheath due to the interaction of an interplanetary TD with the bow shock (e.g., Guo, Lin, & Wang, 2021; Guo, Lin, Wang, & Du, 2018; Lin, 1997; Maynard, Burke, et al., 2007; Maynard, Sonnerup, et al., 2002; Omidi et al., 2009; Pang et al., 2010; Phan, Love, et al., 2011; Phan, Paschmann, et al., 2007). Phan, Paschmann, et al. (2007) and Phan, Love, et al. (2011) have suggested, with both Cluster and THEMIS observations, that reconnection is present in the magnetosheath as a result of the compression of the solar wind current sheet. Both 2D hybrid (Lin, 1997) and 2D MHD (Maynard, Sonnerup, et al., 2002) simulations have demonstrated that magnetic reconnection can be generated as a result of the interaction between a directional TD and the bow shock. 2D (Omidi et al., 2009) and three-dimensional (3D) (Pang et al., 2010) global hybrid simulations have shown the generation of magnetosheath reconnection downstream of the quasi-perpendicular (Q-⊥) shock due to the TD/bow shock interaction. In addition, using a 3D global hybrid simulation, Guo, Lin, Wang, and Du (2018) and Guo, Lin, and Wang (2021) have investigated the interaction of interplanetary directional TDs with the bow shock and the magnetosphere, which results in magnetic reconnection downstream of both Q-⊥ and quasi-parallel (Q-∥) shocks, and the subsequent impacts on the magnetopause flux ropes.

Due to the magnetic field geometry of the Q-∥ shock, the reflected ions can escape along magnetic field lines into the foreshock region in the upstream. Meanwhile, plasma instabilities can be triggered by interaction between these backstreaming ions and the incoming upstream plasma, leading to the development of intense low-frequency waves (Gutynska, Safrankova, & Nemeek, 2009; Lee & Russell, 1994; Shi et al., 2017). Subsequently, these waves are convected with the solar wind back to the magnetosheath, affecting the magnetosheath plasma and field structures (Blanco-Cano, 2006; Gutynska, Šimůnek, et al., 2012; Shevyrev et al., 2006). The solar wind speed, quantified by the upstream magnetosonic Mach number, significantly affects the Q-∥ shock properties because it directly controls the bow shock strength, which in turn affects particle dynamics at the shock front and impacts the wave activity (e.g., Eastwood, Balogh, et al., 2005; Turc et al., 2018). If an upstream interplanetary discontinuity contains a Q-∥ IMF on the sunward side, the waves originated from the Q-∥ shock would affect the evolution of the discontinuity as it is transmitted into the magnetosheath.

Magnetic reconnection has been found in the turbulent plasma downstream of the Q-∥ shock (e.g., Eastwood, Mistry, et al., 2018; Gingell, Schwartz, Eastwood, et al., 2019; Karimabadi et al., 2014; Lu et al., 2020; Øieroset et al., 2017; Phan, Eastwood, et al., 2018; Retinò et al., 2007; Vörös et al., 2017; Yao et al., 2020; Yordanova et al., 2016). Based on MMS spacecraft observations, multiscale structures on the electron scales associated with magnetic reconnection in the turbulent magnetosheath have been reported (Gingell, Schwartz, Eastwood, et al., 2019; Phan, Eastwood, et al., 2018; Yordanova et al., 2016). Ion-scale reconnection has also been observed downstream of the turbulent Q-∥ shock (Cluster: Retinò et al., 2007; THEMIS: Øieroset et al., 2017; MMS: Eastwood, Mistry, et al., 2018; Vörös et al., 2017). Using 2D particle-in-cell (PIC) (Bessho et al., 2019) and 2D hybrid (Gingell, Schwartz, Burgess, et al., 2017) simulations, small-scale turbulent reconnection has been reproduced in the transition region and downstream of a Q-∥ shock. On the other hand, Karimabadi et al. (2014) carried out a 2D global hybrid simulation by imposing an RD to the bow shock and they found that foreshock bubbles are formed due to the interaction of the RD with the shock reflected ions and magnetic islands are present downstream of the turbulent Q-∥ shock, but the interaction of an RD with the bow shock-magnetosphere was rarely investigated. Using a 3D global hybrid simulation, Lu et al. (2020) suggested that the ion-scale magnetosheath reconnection can occur downstream of the Q-∥ shock itself as the large-amplitude shock intrinsic electromagnetic waves are compressed. Recently, reconnection has been observed by MMS spacecraft as an interplanetary directional discontinuity is crossing the Q-⊥ shock (Hamrin et al., 2019), but it is difficult to determine what type of discontinuity is observed. The above studies indicate that magnetic reconnection can occur not only at the magnetopause or in the magnetotail, but also in the extended volume of the magnetosheath and the bow shock. However, it is not understood whether magnetic reconnection can be generated downstream of the Q-∥ shock by interaction between an interplanetary RD and the bow shock-magnetosheath system. Moreover, it is still unclear whether the ion-scale magnetosheath reconnection can be triggered at the Q-∥ shock alone.

In this article, we use a 3D global-scale hybrid simulation to investigate the interaction between an interplanetary RD and the dayside bow shock/magnetosphere. In particular, we examine whether reconnection can be generated downstream of the Q-∥ shock by an external driver in the form of compression of an RD at the bow shock and in the magnetosheath. In the meantime, we also examine whether reconnection can be driven by the spontaneous process in turbulent structures downstream of the Q-∥ shock. The effects of waves originated from the Q-∥ shock on the generation, evolution, and global structure of the magnetosheath flux ropes are investigated. Cases with various magnetic shear angles and solar wind Alfvén speed will be studied.

This study is organized as follows. Section 2 describes our simulation model. The simulation results are presented in Section 3. Summary and discussion are given in Section 4.

2. Simulation Model

Our study is based on a 3D global hybrid simulation model that contains the dayside bow shock-magnetosheath-magnetosphere system (Guo, Lin, Wang, & Du, 2018; Lin & Wang, 2005; Swift, 1996). Detailed numerical scheme of the hybrid code can be found in Swift (1996). In the hybrid simulation, ions are treated as individual particles, and electrons are considered as a massless fluid. Quasi-charge neutrality is assumed in the simulation. A spherical coordinate system (r,θ,φ) is used in the simulation to model the Earth's magnetosphere, which consists of the radial distance r, the polar angle θ relative to the positive GSM z axis, and the azimuthal angle φ from the negative GSM y axis. The Earth is located at the origin. The simulation domain is within the dayside region with $3.5R_E \le r \le 25R_E$. The inner boundary at $r = 3.5R_E$ is treated as a perfectly conducting boundary. The solar wind carrying the IMF in from the frontside (inflow) boundary at $r = 25R_E$. To avoid the singular coordinate lines, two volumes of 20° semicones around the GSM $\pm y$ axes in the equator are cut out from the domain (Lin & Wang, 2005). Outflow boundary conditions are utilized at GSM $x = 0$ and the two semiconic surfaces, which remain open for the plasma to leave the simulation domain. In our simulation the grids are uniformly distributed in the θ and φ directions, while the grid spacing is non-uniform in the r direction, with a total of $n_r \times n_\theta \times n_\varphi = 320 \times 180 \times 220$ grids. The ion inertial length $d_{i0} = c/\omega_{pi0}$ is chosen to be $0.1R_E$ in the solar wind, where ω_{pi0} is the ion plasma frequency, and c is the light speed. A higher spatial resolution with $\Delta r = 0.03R_E$ along the r direction is used around the regions of the bow shock, magnetosheath, and magnetopause.

Noted that the ion kinetic physics is resolved with grid sizes on ion Larmor radius $\sim\rho_i$ or ion inertial length $\sim d_i$ in the hybrid simulation (e.g., Lin, Wang, et al., 2014). Around the bow shock, magnetosheath, and magnetopause, the peak ion density is on the order of $N \approx 2-4N_0$ (where N_0 is the solar wind ion density), and thus the ion inertial length is around $d_i \approx 0.05-0.07R_E$. Therefore, the grid size $\Delta r = 0.03R_E$ used is small enough to resolve the ion kinetic physics. The number of particles per grid is nearly 150–600 in the interested regions of the magnetopause, magnetosheath and bow shock. We have also run a case with more particles (about 1.5 times) per cell. It is found that the results are qualitatively similar. For a run with grid number $n_r \times n_\theta \times n_\varphi = 320 \times 180 \times 220$ and the total particle number $\sim 3.6 \times 10^9$, the wall-clock time consumed is about 160 h when 192 cores are used.

In our self-consistent scheme, the ions are accelerated by the electric and magnetic fields, while the electric field satisfies the generalized Ohm's law combined with Ampere's law, and the magnetic field is advanced with Faraday's law. In the simulation, the magnitude of the unperturbed IMF B_0 is 10 nT, corresponding to a solar wind ion gyrofrequency $\Omega_{i0} \sim 1.0$ Hz, where $\Omega_{i0} = eB_0/m_i$, e is the elementary charge, and m_i is the ion mass. The shape and strength of the bow shock as well as the corresponding structures are found to be qualitatively similar for different choices of d_{i0} (Lin, 1997; Lin & Wang, 2005; Lin, Wang, et al., 2014; Tan et al., 2011).

All variables are normalized by the unperturbed parameters in the solar wind: magnetic field B by the IMF B_0, ion number density N by the solar wind ion density N_0, time t by the solar wind ion gyro-frequency Ω_{i0}^{-1}, and plasma velocity V by the solar wind Alfvén speed V_{A0} ($V_{A0} = B_0 / \sqrt{\mu_0 m_i N_0}$), thermal pressure by $N_0 m_i V_{A0}^2$, electric field by $V_{A0}B_0$, and current density by eN_0V_{A0}. The Alfvénic Mach number is given by $M_A = V_{sw}/V_{A0}$, where V_{sw} is the solar wind speed. In the presentation, the spatial coordinates are expressed in units of R_E.
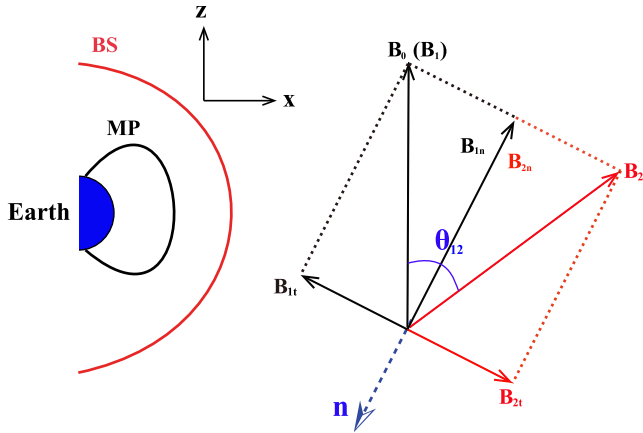
Figure 1. A schematic diagram of the magnetic field configuration of the rotational discontinuity (RD) in xz plane. B_0 is the initial IMF, and B_1 and B_2 denote upstream and downstream magnetic fields of the RD. θ_{12} is an angle between B_1 and B_2. $n = (-\sin(\theta_{12}/2),0,-\cos(\theta_{12}/2))$ is the propagation direction of the RD.

The initial IMF is presumed to be purely northward, with $B_0 = (B_{0x}, B_{0y},B_{0z}) = (0,0,1.0)B_0$, or have a predominant northward B_z component. The solar wind flows along the $-x$ direction carrying the IMF toward the Earth. The magnetopause and the bow shock are formed in a self-consistent manner. An interplanetary RD is imposed to propagate toward the Earth, which interacts with the bow shock at a certain time after the bow shock is fully formed. Across the discontinuity, the physical quantities experience a jump along the discontinuity normal direction, which is the propagation direction of RD. The normal component B_n of magnetic field is constant across the RD, and the RD is allowed to propagate along an arbitrary direction to the bow shock. In our simulation, the propagation direction n of the RD is assumed to point earthward, antiparallel to the normal component of magnetic field, B_n. According to the Rankin-Hugoniot relation, the normal component velocity V_n and tangential flow velocity V_t satisfy

$$\mathbf{V_{n1}} = \mathbf{V_{n2}} = \mathbf{B_n} / \sqrt{\mu_0 m_i N}, \tag{1}$$

$$\begin{aligned}\mathbf{V_{t1}} &= \mathbf{B_{t1}} / \sqrt{\mu_0 m_i N} \\ \mathbf{V_{t2}} &= \mathbf{B_{t2}} / \sqrt{\mu_0 m_i N},\end{aligned} \tag{2}$$

where subscripts 1 and 2 denote the upstream quantities and downstream quantities of the RD, respectively. The quantity B_t denotes the tangential component of the magnetic field. The tangential magnetic fields on both sides of the RD are different only in their directions. The normal component of inflow V_n at the RD is determined from Equation 1. The tangential flow velocity changes according to Equation 2. Across the RD, the rotation angle of the tangential magnetic field has a fixed value $\Delta\Phi = 180°$. The width of the initial RD is assumed to be $10d_{i0}$. We have also run a case with $w = 1d_{i0}$. It is found that the results are qualitatively similar to the case with $w = 10d_{i0}$.

In Figure 1, we present a schematic sketch of the magnetic field configuration of the RD in xz plane. B_1 and B_2 denote upstream magnetic field and downstream magnetic field of the RD. The initial IMF $B_0 = B_1$, and θ_{12} is an angle between B_1 and B_2. RD propagates toward the Earth with propagation direction $n = (-\sin(\theta_{12}/2),0,-\cos(\theta_{12}/2))$. To investigate the effects of RD with different propagation directions n and solar wind Mach numbers M_A on the generation, evolution, and structures of reconnection in the magnetosheath due to the interaction of various RDs with the bow shock and magnetosphere, six cases (1–5) with different n and M_A are presented, as listed in Table 1. In addition, two cases (6 and 7) are also listed in Table 1 in order to illustrate the effects of the initial IMF direction and thus the shock structure on reconnection.

3. Simulation Results

As described in Section 2, the initial IMF in the first six cases is assumed to be $(B_{0x},B_{0y},B_{0z}) = (0,0,1.0)B_0$, pointing northward, which is the upstream field of the incoming RD, that is, $B_1 = B_0$. At time $t = 0$, the RD front is located at a distance corresponding to $x = 40.0R_E$ at $z = 0$, outside the simulation domain. The RD propagates earthward in the solar wind frame. On the basis of the shock-normal angle θ_{Bn}, the collisionless shocks can be categorized as Q-∥ ($\theta_{Bn} < 45°$) and Q-⊥ ($\theta_{Bn} < 45°$) shocks. For the initial IMF configuration before the arrival of the RD, the Q-⊥ shock is located in the region of $|z| < 15.0R_E$ in the noon meridian plane. No shock reflected ions are present upstream of the Q-⊥ shock. As the RD is transmitted through the bow shock, the shock geometry and thus the locations of the Q-∥ and Q-⊥ shocks change in response to the changing of the IMF direction. Figures 2a–2c display the magnetic field strength in the noon meridian plane for cases with downstream $(B_{2x},B_{2y},B_{2z}) = (1.0,0,0)B_0$ (Case 1 with $\theta_{12}=90°$, Figure 2a), $(0.7071,0,-0.7071)$ B_0 (Case 4 with $\theta_{12} = 135°$, Figure 2b), and $(0.9397,0,0.342)B_0$ (Case 5 with $\theta_{12} = 70°$, Figure 2c), obtained at $t = 90\Omega_{i0}^{-1}$. The orange lines in the figure are the magnetic field lines around the bow shock and the red straight lines are along the normal direction of the bow shock at $\theta_{Bn} = 45°$. The locations of the RD fronts

Table 1
Simulation Cases Presented in This Study, With the Various Angles θ_{12} and M_A

Case	$B_1 = B_0$	B_2	$\theta_{12}(°)$	$M_A (V_{A0})$	n
1	(0,0,1.0)	(1.0,0,0)	90	5.6	(−0.7071,0,−0.7001)
2	(0,0,1.0)	(1.0,0,0)	90	3.0	(−0.7071,0,−0.7001)
3	(0,0,1.0)	(1.0,0,0)	90	8.0	(−0.7071,0,−0.7001)
4	(0,0,1.0)	(0.7071,0,−0.7071)	135	5.6	(−0.9239,0,−0.3827)
5	(0,0,1.0)	(0.9397,0, 0.3420)	70	5.6	(−0.5736,0,−0.8192)
6	(−0.7071,0,0.7071)	(1.0,0,0)	135	5.6	(−0.3827,0,−0.9239)
7	(0.3420,0,0.9397)	(1.0,0,0)	70	5.6	(−0.8192,0,−0.5736)

Note. MA is initial solar wind Alfvén Mach number. θ_{12} is the angle between the upstream (B_1) and downstream (B_2) magnetic fields of the rotational discontinuity (RD). The propagation direction of the RD $n = (−\sin(\theta_{12}/2),0,−\cos(\theta_{12}/2))$.
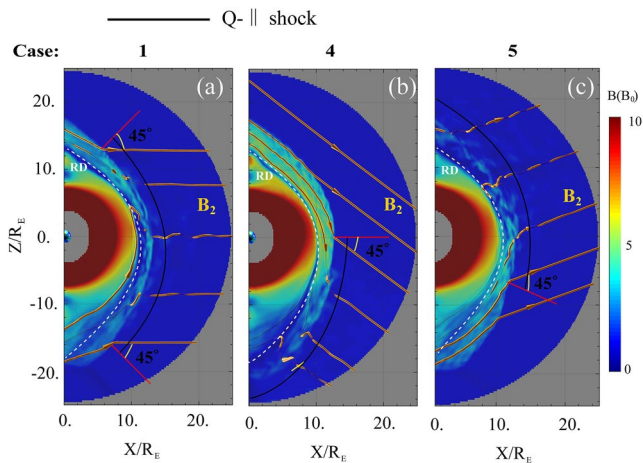
are denoted by the white dashed curves. As shown in Figure 2a, after the passage of the RD, the region of the Q-∥ bow shock is located at $−17.0R_E < z < 13.5R_E$ in Case 1 (denoted by the black curve). In Case 4 with $(B_{2x},B_{2y},B_{2z}) = (0.7071,0,−0.7071)B_0$, the bow shock is dominated by the Q-∥ shock in $z < 0$, as shown in Figure 2b. In addition, Figure 2c displays that in Case 5, the location of the Q-∥ shock is located in $z > −6.5R_E$.

When the interplanetary RD is transmitted through the bow shock and convects toward the magnetopause, magnetosheath reconnection is found to be triggered by interaction between the RD and the bow shock/magnetosheath, forming magnetosheath flux ropes with length of about tens of d_{i0} in the dawndusk direction. As the transmitted RD continuously passes through the magnetopause, new reconnection takes place between the field lines on the sunward side of the RD and the geomagnetic dipole field lines, leading to the generation of flux ropes at the magnetopause, with length of $\sim10d_{i0}$. In addition, no more reconnection is present in the magnetosheath after the RD passes through the dayside magnetopause. The details of the physical processes of the magnetosheath and magnetopause reconnection are presented in the following.
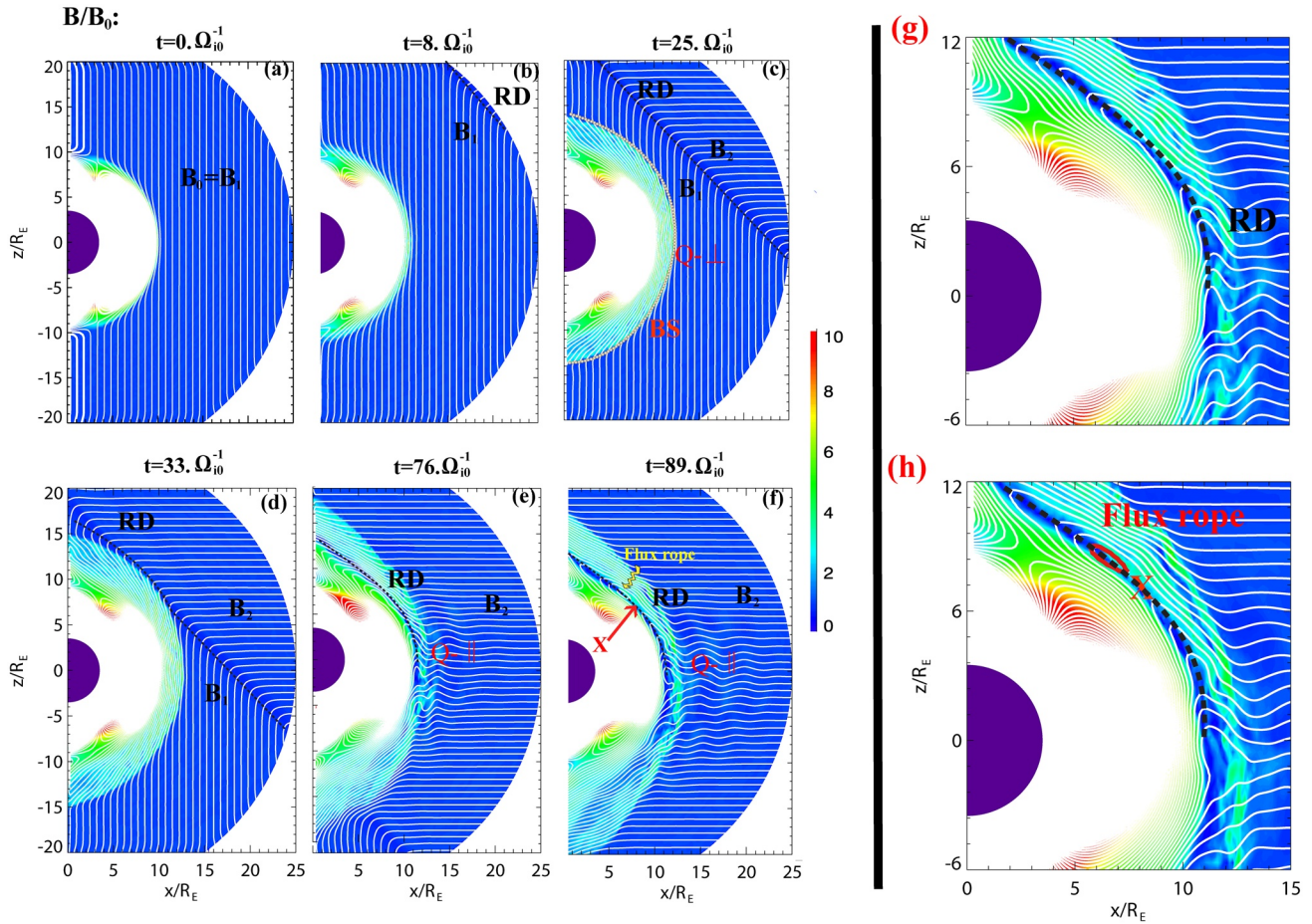

Figure 2. Contour plots of the magnetic field strength in the noon meridian plane for cases with (a) $(B_{2x},B_{2y},B_{2z}) = (1.0,0,0)B_0$ (Case 1), (b) $(0.7071,0,−0.7071)B_0$ (Case 4), and (c) $(0.9397,0,0.342)B_0$ (Case 5) behind the RD obtained at $t = 90\Omega_{i0}^{-1}$. The orange lines are the field lines around the bow shock, and the red lines indicate the normal direction of the bow shock. The locations of the RD fronts are denoted by the white dashed curves.

3.1. Case 1: $\theta_{12} = 90°$ and $M_A = 5.6$

First of all, we present results of interaction of the incoming RD with the bow shock and magnetopause, starting from Case 1, in which the solar wind Alfvén Mach number $M_A = 5.6$ and the propagation direction, n of the RD in the solar wind is 45° relative to the Sun-Earth line, making $(B_{2x},B_{2y},B_{2z}) = (1.0,0,0)B_0$ behind the RD. To illustrate the time evolution while the RD propagates toward the bow shock and the magnetopause, Figures 3a–3f show the magnetic field strength in the noon meridian plane at $t = 0\Omega_{i0}^{-1}, 8\Omega_{i0}^{-1}, 25\Omega_{i0}^{-1}, 33\Omega_{i0}^{-1}, 76\Omega_{i0}^{-1}$, and $89\Omega_{i0}^{-1}$, while the white lines superposed on the contours are the field lines projected onto the 2D plane. The purple hemisphere represents the inner boundary of the simulation. A zoom-in view of Figures 3e and 3f are shown in Figures 3g and 3h, respectively, from $x = 0$ to $15R_E$ and $z = −6R_E$ to $12R_E$. At $t = 0$, the RD is located outside the simulation domain and the initial IMF is purely northward, as shown in Figure 3a. The transmitted RD reaches the north side of the inflow boundary at $t \sim 8\Omega_{i0}^{-1}$, denoted by the black dashed line in Figure 3b.

In the simulation, the bow shock, magnetosheath, and magnetopause are formed in a self-consistent manner at $t \sim 25\Omega_{i0}^{-1}$, as seen in Figure 3c. The location of the bow shock is denoted by the gray dotted line in the noon meridian plane. The geocentric distance of the magnetopause and the

Figure 3. Contour plots of the magnetic field strength in the noon meridian plane at $t = 0\Omega_{i0}^{-1}$, $8\Omega_{i0}^{-1}$, $25\Omega_{i0}^{-1}$, $33\Omega_{i0}^{-1}$, $76\Omega_{i0}^{-1}$, and $89\Omega_{i0}^{-1}$ obtained from Case 1. The magnetic field lines are superposed denoted by white lines. The dashed line denotes the RD location in the magnetosheath. The reconnection "X" point is denoted by symbol "X." The purple sphere represents the inner boundary of the simulation.

bow shock at the subsolar point is about $10.0R_E$ and $13.0R_E$, respectively. Across the bow shock, the magnetic field, ion number density, and thermal pressure increase, while the flow speed decreases. The flow direction diverges to the north and south (not shown). At $t = 25\Omega_{i0}^{-1}$, the RD has propagated into the simulation domain from the inflow boundary, as marked by dashed lines in Figure 3c, across which the IMF direction changes. The RD then reaches the bow shock at $t \sim 33\Omega_{i0}^{-1}$, as seen in Figure 3d in which the curved black dashed line marks the bow shock. We note that no reconnection occurs inside the RD before it interacts with the bow shock.

As the RD is transmitted through the bow shock at $t = 76\Omega_{i0}^{-1}$, it is dragged tailward and poleward by the magnetosheath flows, forming a paraboloidal-shaped structure. The RD is compressed by the initially Q-⊥ bow shock and then the magnetosheath, similar to that in the TD/bow shock interaction as reported by Pang et al. (2010), Guo, Lin, Wang, and Du (2018), and Guo, Lin, and Wang (2021). The transmitted RD is the thinnest around $z = 7.0R_E$, where it was first in contract with the bow shock. Southward of the equator, however, the RD gradually becomes weaker because the southward magnetosheath flows drag the field lines in the way that they straighten the field lines across the RD, as shown in Figures 3e and 3g. Meanwhile, the IMF has changed to $(B_{2x}, B_{2y}, B_{2z}) = (1.0,0,0)B_0$ in the upstream solar wind. Correspondingly, the shock structure changes from being Q-⊥ to Q-∥ around the subsolar region (Figure 2a). Upstream of the Q-∥ shock, there exist large-amplitude low-frequency electromagnetic perturbations. These foreshock waves are generally found to be excited by the interaction between the backstreaming reflected ions and the incoming solar wind (e.g., Hoppe et al., 1983; Lin & Wang, 2005; Liu et al., 2019; Russell & Hoppe, 1983; Scholer
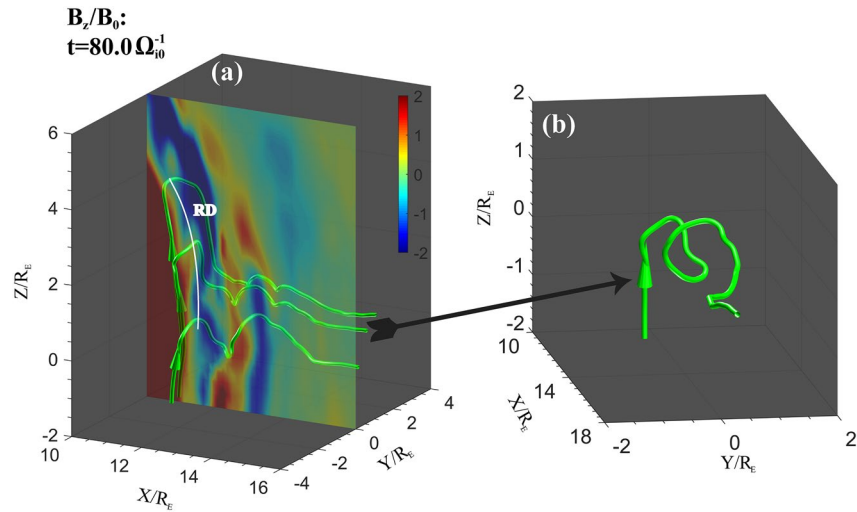
Figure 4. (a) Magnetic field line configuration around the equator at $t = 80\Omega_{i0}^{-1}$. The green field lines are the magnetic field lines. (b) A zoom-in view. The contour in the noon meridian plane shows the B_z component of the magnetic field.

et al., 1990; Shi et al., 2017), which results in the waggled magnetic field lines in Figure 3e. Subsequently, the waves generated upstream of the Q-∥ shock penetrate into the magnetosheath, leading to the bending and squeezing of the field lines in the RD, which in turn play an important role in facilitating magnetic reconnection inside the RD in the magnetosheath. The details of these waves will be shown in Figures 4 and 5. At $t = 89\Omega_{i0}^{-1}$, magnetic flux ropes are present in the transmitted RD in the magnetosheath, and they are located where an "island" like structure is present in the 2D projection of field lines, marked by the red line in Figure 3h. The reconnection region is located around $(x,z) = (8.0,7.5)R_E$ in the noon meridian plane southward of the flux rope, denoted by the symbol "X" in Figures 3f and 3h. No magnetosheath reconnection is found on the southward side of the equator, where the RD becomes wide. We have included two supplemental movies to show the time evolution of the magnetic field strength and ion density as well as the field line configuration (see Movies S1 and S2).

The low-frequency waves originated from the Q-∥ shock significantly affect the evolution of the RD in the magnetosheath. Figure 4a shows the magnetic field line configuration around the equator, obtained from Case 1 at $t = 80\Omega_{i0}^{-1}$. The green lines are the magnetic field lines around the Q-∥ shock. A zoom-in view of the field line around the Q-∥ shock is plotted in Figure 4b. The contour in the noon meridian plane shows the B_z component. The location of RD is denoted by the solid white line. It is found that the low-frequency waves possess a nearly circular polarization of magnetic field, leading to the green field line configuration in Figure 4b. At the location of the RD in the magnetosheath, these waves cause the bending and squeezing of the field lines of the RD (Figures 4a and 4b), leading to the generation of a thin current sheet with a larger magnetic shear angle inside the RD and, in turn, magnetic reconnection inside the RD in the magnetosheath.

The low-frequency wave properties upstream of the Q-∥ shock are also investigated. Figure 5a displays the time evolution of (a1) the magnetic field strength B, (a2) the ion density N_i, the magnetic field components (a3) B_x, (a4) B_y (blue) and B_z (red), and the electric field components (a5) E_x (black), E_y (blue) and E_z (red), measured in Case 1 by a virtual spacecraft positioned at $(x,y,z) = (15.4,0,0)R_E$ (in the foreshock region). The associated power spectrum of the B_y component is depicted in Figure 5b. Noted that in this case of a radial IMF, upstream the magnetic field fluctuates around $(B_x,B_y,B_z) = (1,0,0)B_0$, as shown in Figures 5a (a3) and 5a (a4). The ion density is seen to fluctuate in a nearly positive correlation with the magnetic field, as shown in Figures 5a (a1) and 5a (a2), consistent with the diamagnetic cavities simulated by Lin and Wang (2005). Significant fluctuations are found in all components of the magnetic field and electric field, especially in the y and z components, as shown in Figures 5a (a4) and 5a (a5). Moreover, there is an almost 90° phase difference between the y components and the z components. During the time $t < 118.\Omega_{i0}^{-1}$, the amplitude of B_y and B_z is about $0.7B_0$. In $t > 118.\Omega_{i0}^{-1}$, the amplitude is decreased, probably due to the change
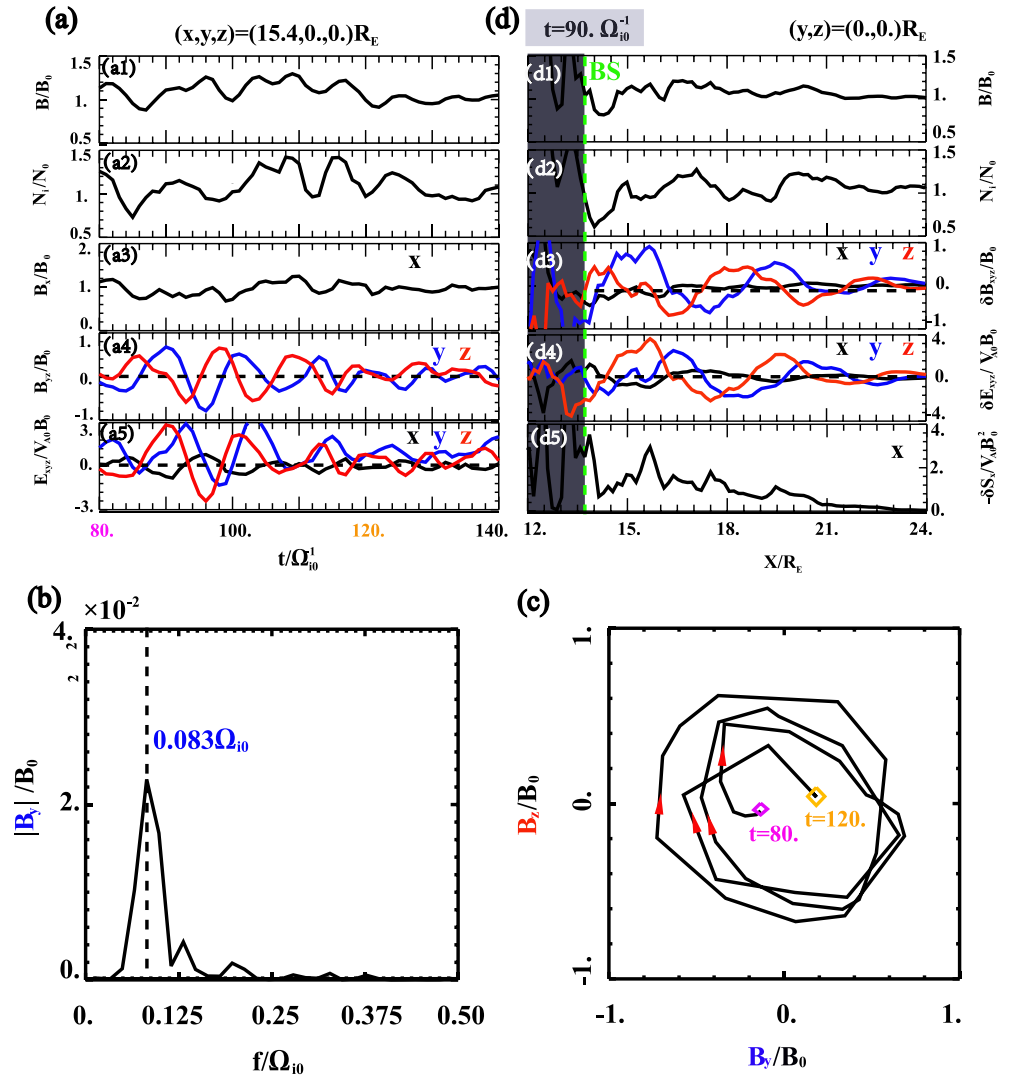
Figure 5. (a) The time series of (a1) the magnetic field strength B, (a2) the ion density N_i, the magnetic field components (a3) B_x, (a4) B_y (blue) and B_z (red), and the electric field components (a5) E_x (black), E_y (blue) and E_z (red), measured in Case 1 by virtual spacecraft positioned at $(x,y,z) = (15.4,0,0)R_E$ (in the foreshock region), (b) its associated power spectrum of the B_y component. (c) Hodogram of the waves in $B_y - B_z$ plane from $t = 80.\Omega_{i0}^{-1}$ to $t = 120.\Omega_{i0}^{-1}$. (d) The spatial cuts of (d1) the magnetic field strength B, (d2) the ion density N_i, the magnetic field fluctuations (d3) δB_x (black), δB_y (blue) and δB_z (red), the electric field fluctuations (d4) δE_x (black), δE_y (blue) and δE_z (red), and (d5) Poynting flux component $-\delta S_x$ along the Sun-Earth line in the sunward direction, obtained at $t = 90.\Omega_{i0}^{-1}$. The green dashed line marks the location of the subsolar Q-$\parallel$ shock.

of the Q-$\parallel$ shock structures. Noted that the solar wind ion gryofrequency $\Omega_{i0} \sim 1.0$ Hz in our simulation for a typical IMF $B_0 = 10.nT$. It is seen from Figure 5b that only the wave power peaks at frequency around $0.083\Omega_{i0}$ (~83 mHz). Noted that the phase speed direction of the waves is along $-x$ toward the Earth in the simulation frame, while it points to the Sun in the solar wind plasma frame. Using a minimum variance analysis (Sonnerup & Scheible, 1998), we find that the waves nearly propagate along the magnetic field direction (B_x). We then plot magnetic field hodogram in the B_y-B_z plane to examine its polarization. As shown in Figure 5c, the waves are right-hand (left-handed) in solar wind plasma (in the simulation) frame of reference from $t = 80.\Omega_{i0}^{-1}$ to $t = 120.\Omega_{i0}^{-1}$. The upstream electromagnetic waves are found to be consistent with the beam whistler modes, which have been investigated in previous hybrid simulations (e.g., Lin & Wang, 2005).

B/B₀:
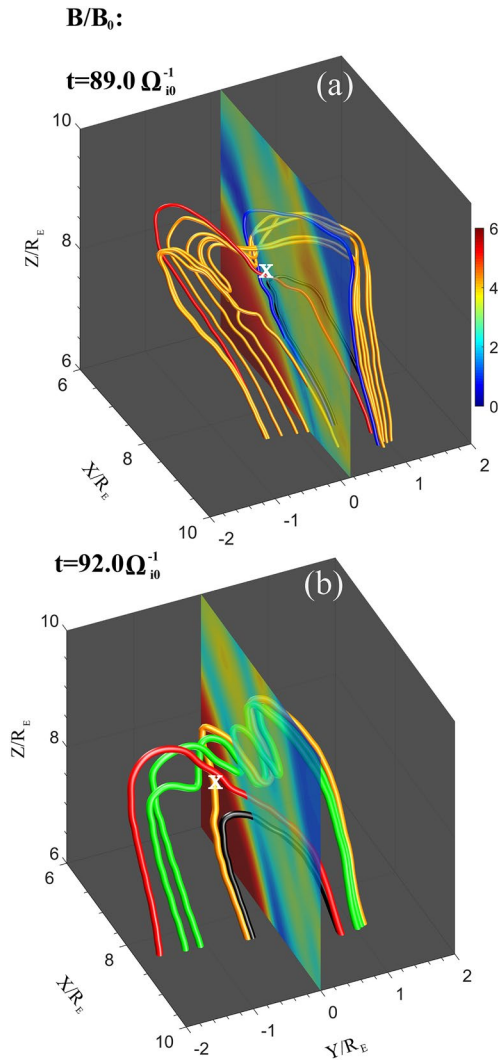
Figure 6. Magnetic field line configuration in a zoom-in view around the magnetosheath X point at (a) $t = 89\Omega_{i0}^{-1}$ and (b) $t = 92\Omega_{i0}^{-1}$. The orange and green field lines represent the flux rope inside the RD in the magnetosheath, the red and blue field lines are the magnetic field lines outside the magnetic merging layer, and the black ones mark the reconnected field lines near the X points. Contour plots show the magnetic field strength in the $y = 0$ and $y = -0.3R_E$ plane.

Figure 5d displays the spatial cuts of (d1) the magnetic field strength B, (d2) ion density N_i, magnetic field fluctuations (d3) δB_x (black), δB_y (blue) and δB_z (red), electric field fluctuations (d4) δE_x (black), δE_y (blue) and δE_z (red), and (d5) the Poynting flux component $-\delta S_x$ along the Sun-Earth line in the sunward direction, obtained at $t = 90.\Omega_{i0}^{-1}$. The central position of the subsolar Q-∥ shock ($\sim x = 13.7R_E$), which is indicated by the green dashed line in Figure 5d, can be identified by the sharp gradients of the magnetic field strength and ion density (Figures 5d (d1) and 5d (d2)). The wavelength of the waves is nearly $\lambda \approx 4.1R_E$ ($\sim 41d_{i0}$), based on the field fluctuations in Figures 5d (d3) and 5d (d4). The Poynting flux component, δS_x, is about $-2.0V_{A0}B_0^2$ (Figure 5d (d5)). For a typical IMF of 10 nT and a solar wind density of 6 cm^{-3}, the unit power density $V_{A0}B_0^2$ is 7.1×10^{-6} W/m^2. Therefore, δS_x averaged in the simulated foreshock region is about -1.4×10^{-5} W/m^2. Moreover, the Doppler shift of the frequency $\Delta\omega = k_x V_{SW}$ is $\sim 0.705\Omega_{i0}$, where $k_x = 2\pi/\lambda$. Therefore, the wave frequency in the solar wind plasma frames is estimated to be $f_r = f - \Delta\omega/2\pi \sim -0.029\Omega_{i0}$ (~ 29 mHz), where f is the frequency in the simulation frame. This negative sign of the wave frequency is correlated to the reversal of the phase speed direction in the simulation frame (Narita et al., 2004).
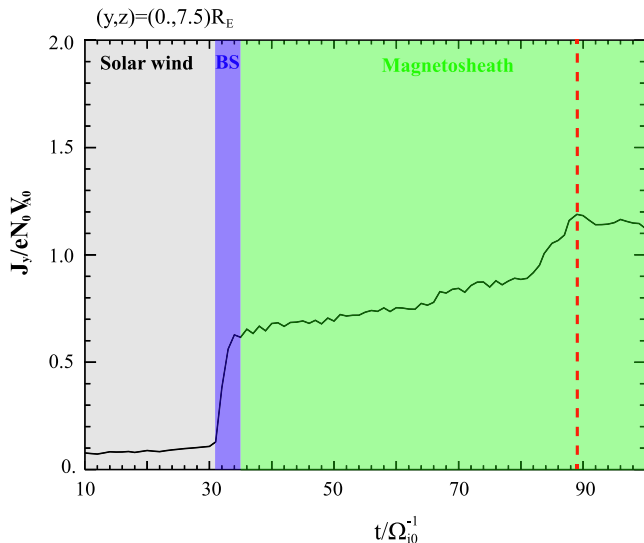
To investigate the formation process of the magnetic flux ropes inside the RD in the magnetosheath, Figure 6 displays the magnetic field line configuration of the flux rope at (Figure 6a) $t = 89\Omega_{i0}^{-1}$ and (Figure 6b) $t = 92\Omega_{i0}^{-1}$. The contours show the magnetic field strength in the xz plane at (Figure 6a) $y = 0$ and (Figure 6b) $y = -0.3R_E$. The orange field lines denote the reconnected field lines (flux rope), and the red and blue field lines represent the no reconnected field lines around the magnetic merging layer at $t = 89\Omega_{i0}^{-1}$. The green field lines reveal the magnetosheath flux rope inside the RD at $t = 92\Omega_{i0}^{-1}$. The black lines mark the reconnected field lines near the reconnection X sites. In Figure 6a, the point denoted by "X" is an X point, identified in a similar way as described in work of Guo, Lin, Wang, Vines, et al. (2020), which is the same "X" point shown in Figure 3f. The magnetic topology of the X point is further confirmed by using the topological degree method (Greene, 1992; Guo, Lin, Wang, & Du, 2018). Figure 6a shows that reconnection takes place between the two field lines denoted by the red and blue color, resulting in the generation of the orange and black field lines at $t = 89\Omega_{i0}^{-1}$. It is found that reconnection has taken place between the field lines similar to the orange and the red lines around $(x,y,z) = (7.9, -0.3, 7.7)R_E$ at $t = 92\Omega_{i0}^{-1}$, resulting in the generation of the green and black field lines, as shown in Figure 6b. An extended flux rope is formed by such reconnection process.

The overall structures of various physical quantities around the "X" point in Figure 6 are also studied. Figure 7 exhibits the zoomed-in contour plots of (Figure 7a) the component j_y of current density (Figure 7b), the component B_y (Figure 7c), the electric fields $\mathbf{E'_x} = \mathbf{E_x} + (\mathbf{V_i} \times \mathbf{B})_x$ and (Figure 7d) $\mathbf{E'_y} = \mathbf{E_y} + (\mathbf{V_i} \times \mathbf{B})_y$ (Figure 7e) the ion bulk flow component V_{iz} (Figure 7f), $\mathbf{J_y} \cdot \mathbf{E'_y}$ (Figure 7g), $J \cdot E'$ (Figure 7h), the ion density N_i, and (Figure 7i) the ion temperatures $T_\parallel$ and (Figure 7j) $T_\perp$, from $x = 0$ to $12.0R_E$ and $z = 4.0R_E$ to $16.0R_E$, where black lines superposed on the contours are the field lines projected onto the 2D noon meridian plane. By shock compression and convection compression processes at the bow shock and in the magnetosheath (Guo, Lin, & Wang, 2021; Guo, Lin, Wang, & Du, 2018; Pang et al., 2010), a thin current sheet with width of $\sim 3.0d_{i0}$ is formed above the equator in the magnetosheath, as shown in Figure 7a. The evolution of the current density inside the RD will be elaborated in Figure 8. The reconnection magnetic field is $B_r \approx B_z \approx 2.8B_0$ (not shown). There is a guide field around the "X" point, with a value of $\sim 0.2B_0$. Moreover, quadrupolar

t=89.0Ω$_{i0}^{-1}$:
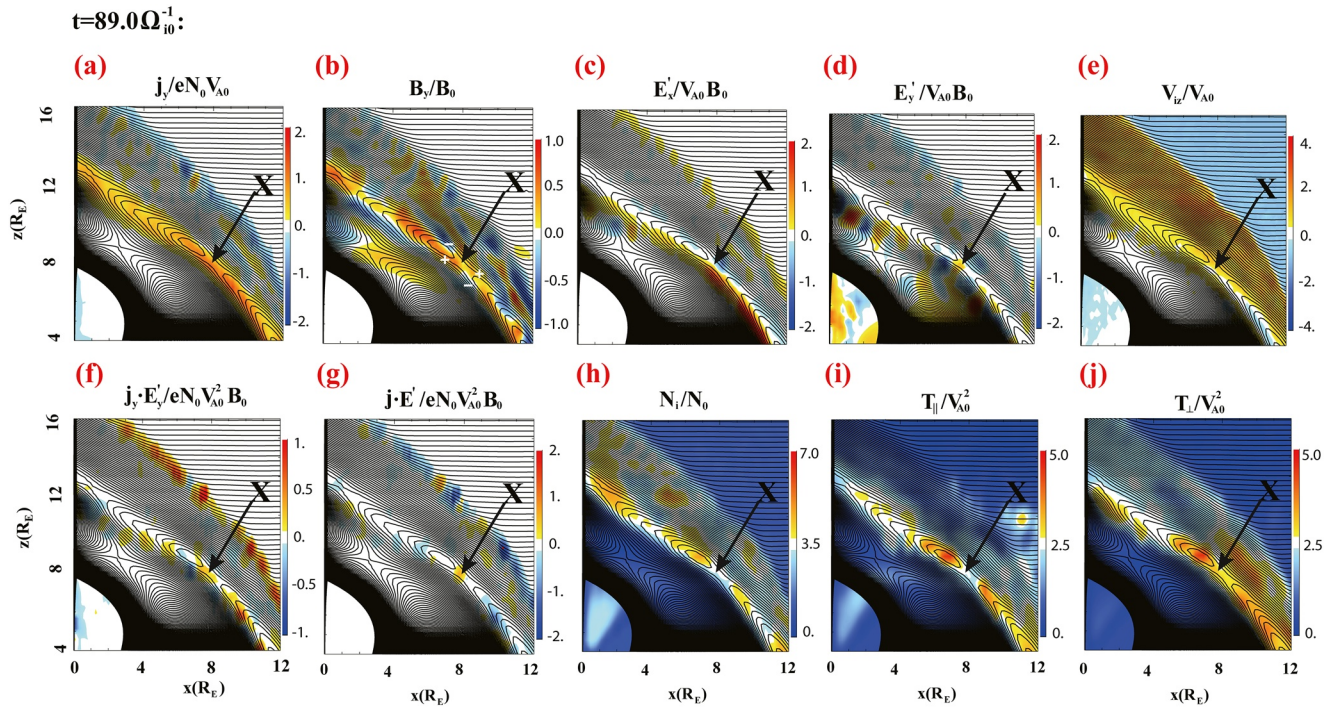
Figure 7. The contour plots of zoomed-in structures around the *X* line in the noon meridian plane at $t = 89\Omega_{i0}^{-1}$. Here (a–j), correspond to the component J_y, the component B_y, the Hall electric field $\mathbf{E'_x} = \mathbf{E_x} + \left(\mathbf{V_i} \times \mathbf{B}\right)_x$, $\mathbf{E'_y} = \mathbf{E_y} + \left(\mathbf{V_i} \times \mathbf{B}\right)_y$, the ion bulk flow component V_{iz}, $\mathbf{J_y} \cdot \mathbf{E'_y}$, $J \cdot E'$, ion density N_i, the ion temperature $T_\parallel$ and $T_\perp$, respectively.

perturbations $\delta B_y \sim 0.5B_0$ relative to the guide field are present, as denoted by the signs of positive and negative in the vicinity of the "*X*" point in Figure 7b, which is consistent with the Hall effects due to the ion inertial effects (e.g., Pritchett, 2001). The Hall electric field $\mathrm{E'_x}$ changes from positive to negative in the sunward direction across the "*X*" point in Figure 7c, which is due to the charge separation effects in the Hall physics. Figure 7d reveals a positive value $\sim 0.36V_{A0}B_0$ of the reconnection electric field $\mathrm{E'_y}$ is present around the "*X*" point. Moreover, wave structures consistent with the Alfvén waves are also found around the reconnection region, propagating in opposite directions away from the *X* line. Alfvén waves generated from the reconnection region have been investigated in previous hybrid simulations (e.g., Cheng et al., 2020; Wang, Lin, et al., 2019).

In Figure 7e, the presence of outflow reconnection jets with V_{iz} of opposite signs can be seen on the two sides of the "*X*" point, pointing away from the "*X*" point. At this moment, the "*X*" point moves northward with the ambient magnetosheath flow (e.g., Guo, Lin, Wang, Vines, et al., 2020), with a speed of $\sim 1.0V_{A0}$. The outflow velocity northward of the "*X*" point is northward, $\sim 1.7V_{A0}$, larger than the speed of the "*X*" point. On the southward side of the "*X*" point, the outflow speed is also northward, $\sim 0.1V_{A0}$, smaller than the speed of the "*X*" point. Therefore, there exists an outflow jet away from the "*X*" point, with a speed of $\sim 0.8V_{A0}$.

Figure 8. The evolution of the current density J_y inside the RD, at $(y,z) = (0.,7.5)R_E$, as a function of time.

The quantity $\mathbf{J_y} \cdot \mathbf{E'_y}$ and $J \cdot E'$ have a positive value around the "*X*" point in Figures 7f and 7g, which indicates that the magnetic energy is converting into plasma kinetic energy (e.g., Angelopoulos et al., 2008; Birn et al., 2001; Nagai et al., 1998; Wang, Nakamura, et al., 2017). Figure 7h shows that the ion density has a significant enhancement in the flux rope (projected as an island in the 2D plane) and the outflow region. Around
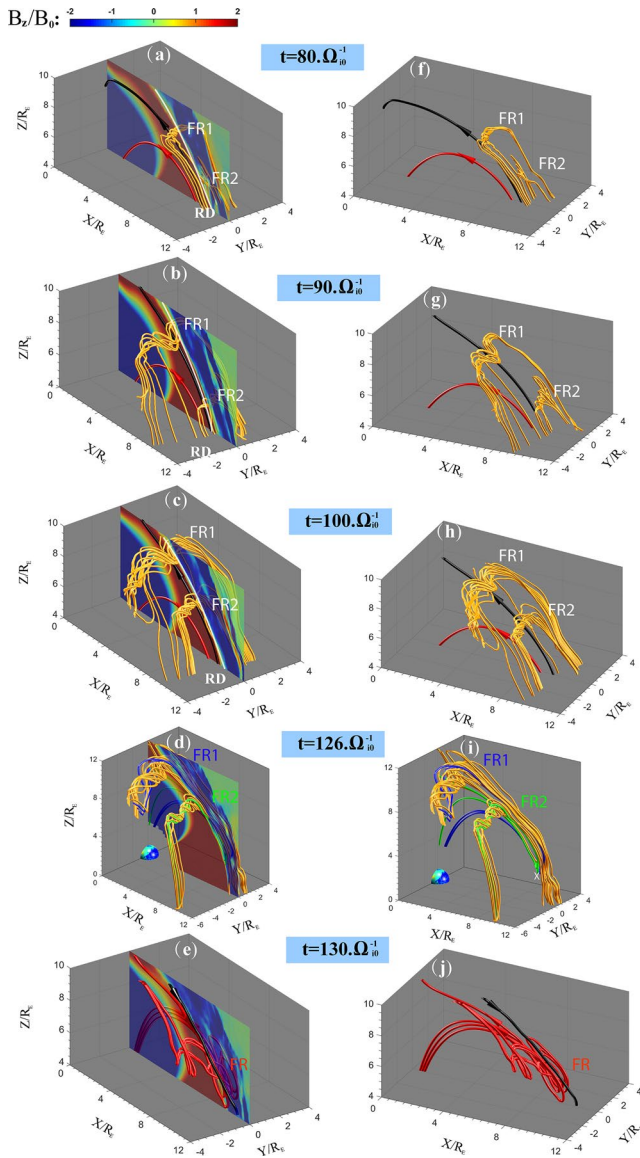
Figure 9. (Left) Contours of the magnetic field strength in the noon meridian plane obtained at (a) $t = 80\Omega_{i0}^{-1}$, (b) $90\Omega_{i0}^{-1}$, (c) $100\Omega_{i0}^{-1}$, (d) $126\Omega_{i0}^{-1}$, and (e) $130\Omega_{i0}^{-1}$. (Right) (f–j) Magnetic field line configuration in a zoom-in view. The orange lines denote the magnetosheath flux ropes inside the RD, the blue and green lines denote the newly formed field lines of the flux ropes, the red lines mark the field line at the magnetopause, and the black lines represent the magnetic field lines outside the magnetopause. Two magnetosheath flux ropes are denoted by "FR1" and "FR2," and magnetopause flux rope is marked by "FR.".

the "X" point, the ion density N_i is about is about 3.0n_0, and temperatures $T_\parallel$ and $T_\perp$ are about $2.5V_{A0}^2$ and $4.2V_{A0}^2$, respectively. Corresponding to the density enhancement, ion temperature enhancement is also found, with greater enhancement in $T_\parallel$ than $T_\perp$, as shown in Figures 7i and 7j. However, since the background ion temperature $T_\perp > T_\parallel$ downstream of the bow shock, the ratio $T_\parallel / T_\perp \sim 0.6$ in the reconnection region, is still less than 1. All the above evidence is consistent with the occurrence of magnetic reconnection. In the reconnection region, the Walen relation of the single transmitted RD is not satisfied.

Noted that the reconnection magnetic field $B_r \approx B_z \approx 2.8B_0$, the ion density $N_i \approx 3.0N_0$, and the reconnection electric field $E_y' \sim 0.36V_{A0}B_0$ around the "X" point. Thus, the reconnection rate is about $E_y' / V_A B_r \sim \dfrac{E_y'}{V_{A0}B_0} \cdot \dfrac{B_0^2}{B_z^2} \sqrt{\dfrac{N_i}{N_0}} \simeq 0.08$, where $V_A = B_r / \sqrt{\mu_0 m_i N_i}$. The reconnected flux is about $0.13B_0R_E^2$ at $t = 89\Omega_{i0}^{-1}$, which is calculated by integrating the normal magnetic flux between the major X point and the neighboring major O point. However, the time evolution of the reconnected flux is very difficult to calculate due to the motion of the reconnection site.

Figure 8 depicts the evolution of the current density J_y inside the RD during its interaction with the bow shock and the magnetosheath, at $(y,z) = (0.,7.5)R_E$, as a function of time. It is found that J_y is nearly constant while the RD is in the solar wind, with a positive value $\sim 0.09eN_0V_{A0}$. At $t \approx 33.0\Omega_{i0}^{-1}$, the interplanetary RD interacts with the bow shock, where the RD is significantly compressed. This time duration when the RD is interacting with the bow shock is labeled as "BS" in the figure. The current density J_y increases by a factor of ~ 7.0, to $\sim 0.63eN_0V_{A0}$ after the RD crossing the bow shock. Since the magnetic field only increases by a factor of ~ 2.0 across the shock, the stronger enhancement of J_y indicates that the thickness of RD is reduced to about $1/3.5$ of the original value. In the magnetosheath, the RD is further compressed by the convection compression process and J_y continues to increase as the RD propagates toward the Earth. At $t \approx 89.0\Omega_{i0}^{-1}$, denoted by the vertical red dashed line, J_y reaches a peak value of $\sim 1.2eN_0V_{A0}$, which is also found in Figure 7a. Around this moment, magnetosheath reconnection takes place at $(x,y,z) = (8.0,0.,7.5)R_E$ inside the RD downstream of the Q-∥ shock, denoted by the "X" point in Figure 7.

To illustrate the time evolution of magnetosheath flux ropes, Figures 9a–9e display the contours of the B_z component in the noon meridian plane, as well as the corresponding 3D field lines (Figures 9f–9j) downstream of the bow shock from Cases 1 at $t = 80\Omega_{i0}^{-1}$, $90\Omega_{i0}^{-1}$, $100\Omega_{i0}^{-1}$, $126\Omega_{i0}^{-1}$, and $130\Omega_{i0}^{-1}$. The locations of the RD in the magnetosheath are denoted by the curved white lines in Figures 9a–9c, where the B_z component varies from positive value to negative value. The orange field lines mark the flux ropes inside the RD in the magnetosheath from $t = 80\Omega_{i0}^{-1}$ to $t = 126\Omega_{i0}^{-1}$,
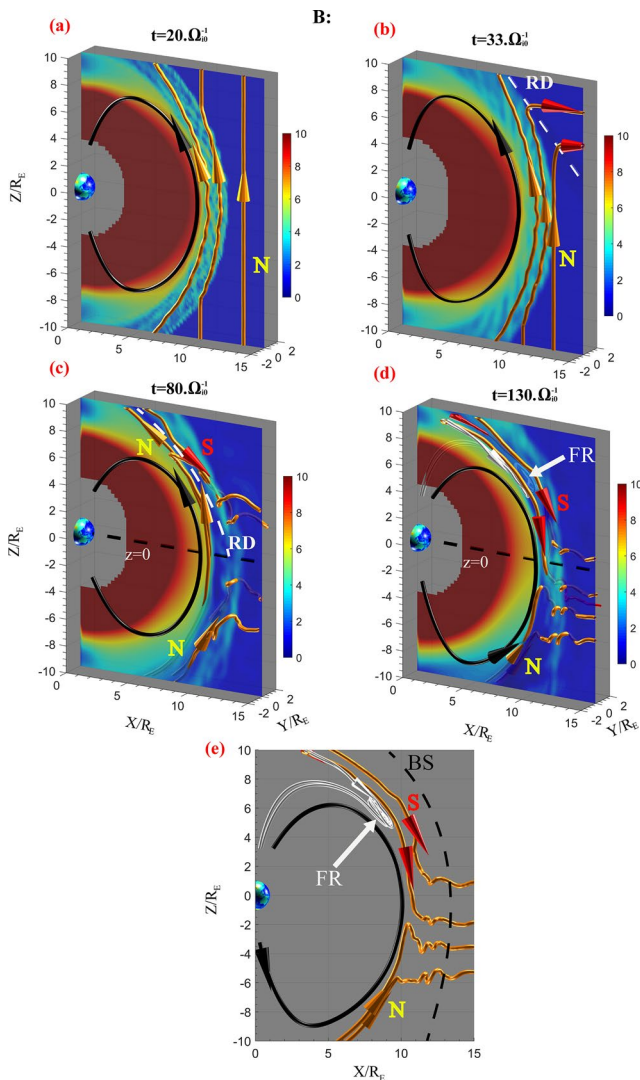
the blue and green field lines denote the newly formed field lines of the flux ropes, the red lines represent the field lines at the magnetopause, and the black lines are the field lines outside the magnetopause. The arrows on the colored field lines indicate the directions of the magnetic field. In the whole process of the RD crossing the bow shock and passing through the dayside magnetopause, two magnetosheath flux ropes are found above the equator inside the RD, as marked by "FR1" and "FR2" in this figure. At $t = 80\Omega_{i0}^{-1}$, the two flux ropes are generated around $(x,z) = (7.0,7.9)R_E$ and $(x,z) = (9.5,5.3)R_E$ in the noon meridian plane, denoted by "FR1" and "FR2," respectively, as shown in Figures 9a and 9f. The extensions of the flux

Figure 10. The time evolution of the field line configuration outside the magnetopause on the northward side of the equator, at (a) $t = 20.\Omega_{i0}^{-1}$, (b) $33.\Omega_{i0}^{-1}$, (c) $80.\Omega_{i0}^{-1}$, and (d) $130.\Omega_{i0}^{-1}$. The contours in the $y = 0$ plane show the magnetic field strength. The black lines represent the field lines around the magnetopause, the orange ones mark the open field lines outside the magnetopause, and the white line denotes the flux rope at the magnetopause. The arrows on the colored field lines indicate the directions of the magnetic field.

ropes along the y direction are about $30d_{i0}$ ("FR1") and $10d_{i0}$ ("FR2"). Subsequently, the two flux ropes move poleward with the magnetosheath flows. At $t = 90\Omega_{i0}^{-1}$, the two flux ropes have moved to $(x,z) = (6.3,8.7)$ R_E ("FR1") and $(x,z) = (8.8,5.9)R_E$ ("FR2"), and their lengths are about $45d_{i0}$ and $20d_{i0}$, as shown in Figures 9b and 9g. At $t = 100\Omega_{i0}^{-1}$, the flux ropes "FR1" and "FR2" have moved to $(x,z) = (5.1,9.3)R_E$ and $(7.7,7.1)R_E$, respectively, as indicated in Figures 9c and 9h. The lengths of "FR1" and "FR2" have further increased to about $60d_{i0}$ and $40d_{i0}$.

No reconnection is present at the magnetopause before the RD reaches the magnetopause. At about $t = 126\Omega_{i0}^{-1}$, the two flux ropes reach and interact with the dayside magnetopause. Noted that the propagation direction of the RD is $n = (-0.7071,0,-0.7071)$ in Case 1. The magnetic field direction change due to the RD, from northward to southward, at the magnetopause first occurs around $z \approx 4.0R_E$, where magnetopause reconnection first takes places (denoted by the white label "X"), resulting in the green and blue field lines wrapped inside the flux ropes "FR1" and "FR2," (Figures 9d and 9i). The evolution of the magnetic field directions just outside the magnetopause will be shown in Figure 10. Subsequently, the two flux ropes move out of the tail-side boundary at about $t = 130\Omega_{i0}^{-1}$. When the RD impacts the dayside magnetopause, the magnetic field outside the magnetopause behind the RD changes from northward to southward on the north side of the equator (denoted by the black field lines in Figures 9e and 9j), while it still points northward on the south side of the equator for the time being.

In the meantime, it is found that at $t = 130\Omega_{i0}^{-1}$, magnetic reconnection has taken place at the magnetopause above the equator where the magnetic field is nearly antiparallel on the two sides of the magnetopause current layer, resulting in the generation of the magnetopause flux ropes (denoted by "FR") with a size of $\sim 10d_{i0}$ in the dawn-dusk direction, denoted as the red field lines in Figures 9e and 9j. No magnetopause reconnection can be found on the south side of the equator in the entire run.

To illustrate the dynamic evolution of the magnetic field direction outside the magnetopause on the northward side of the equator due to the arrival of the RD, Figure 10 shows the field line configuration around the magnetopause in the noon meridian plane at (Figure 10a) $t = 20.\Omega_{i0}^{-1}$ (Figure 10b), $33.\Omega_{i0}^{-1}$ (Figure 10c), $80.\Omega_{i0}^{-1}$, and (Figures 10d and 10e) $130.\Omega_{i0}^{-1}$. The contours in the $y = 0$ plane show the magnetic field strength. The black line represents the field line around the magnetopause, the orange ones mark the open field lines outside the magnetopause, and the white line denotes a flux rope at the magnetopause. The arrows on the colored field lines indicate the directions of the magnetic field. At $t = 20.\Omega_{i0}^{-1}$, the field lines outside the magnetopause point northward, denoted by the orange label "N" in Figure 10a. The RD has reached the bow shock at $t = 33.\Omega_{i0}^{-1}$, as seen in Figure 10b. The magnetic field outside the magnetopause is still northward before the arrival of the RD. As the RD is transmitted through the bow shock and propagates toward the Earth, a paraboloidal-shaped structure of the RD is formed, as marked by the orange field lines at $t = 80.\Omega_{i0}^{-1}$ in Figure 10c. On the earthward side of the RD above the equator, the magnetic field changes to southward behind the RD (denoted by the red label "S"). Around $t = 130.\Omega_{i0}^{-1}$, the RD passes through the magnetopause, thus the magnetic field outside the magnetopause in the northern hemisphere has turned to southward (Figures 10d and 10e). In the meantime, magnetopause reconnection has taken place between the northward magnetopause field lines and the southward magnetosheath field lines above
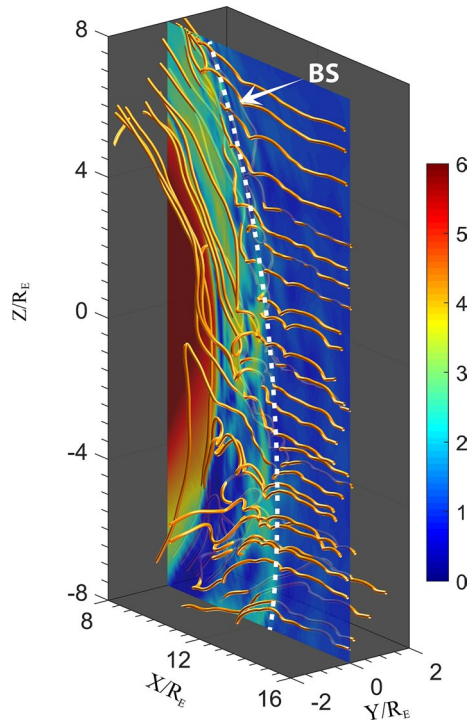
Figure 11. Magnetic field line configuration in a zoom-in view around the Q-∥ shock, obtained from Case 1 at $t = 160\Omega_{i0}^{-1}$. The contour in xz plane displays the magnetic field strength.

the equator, resulting in the generation of the flux rope denoted by the white field line, as shown in Figures 10d and 10e.

No magnetosheath reconnection is found downstream of the Q-∥ shock after the RD passes through the magnetopause at $t \approx 130\Omega_{i0}^{-1}$. As an example, Figure 11 displays a zoom-in view of the field line configuration around the subsolar region, obtained from Case 1 at $t = 160\Omega_{i0}^{-1}$. The orange lines are the magnetic field lines around the Q-∥ shock, and a curved white dashed line marks the location of the bow shock. The contour plot in the noon meridian plane shows the magnetic field strength. It is found that the waggled magnetic field lines are present downstream of the Q-∥ shock due to the low-frequency turbulence in the magnetosheath. However, no reconnection flux ropes are found in the entire magnetosheath at $t > 130\Omega_{i0}^{-1}$. Similarly, no reconnection is present downstream of the Q-∥ shock in Case 3 with a larger Alfvén Mach number $M_A = 8.0$ after the RD reaches the magnetopause. Our simulations indicate that large-scale magnetosheath reconnection is not driven by the spontaneous process in the turbulent structures downstream of the Q-∥ shock.

3.2. Cases 1–3 With Various Alfvén Mach Number M_A

Solar wind Alfvén Mach number has a great effect on the excitation of low-frequency waves in the foreshock of the Q-∥ shock, which in turn plays an important role in the bending of field lines around the RD in the magnetosheath. To illustrate the effects of the solar wind Alfvén Mach number M_A on the generation of low-frequency waves, Figures 12a–12c show the magnetic field line configuration in a zoom-in view around the Q-∥ shock, for $M_A = 3.0$ (Case 2, Figure 12a), 5.6 (Case 1, Figure 12b), and 8.0 (Case 3, Figure 12c), assuming $\theta_{12} = 90°$ and the initial IMF is purely northward. The contours in the figure display B_z in the noon meridian plane. The green lines denote the field lines around the Q-∥ shock. In Case 2 with $M_A = 3.0$, the geocentric distances of the magnetopause and the bow shock are about $12.3R_E$ and $15.4R_E$ at the subsolar point, respectively. In Case 3 with $M_A = 8.0$, however, they have shifted inward to $8.4R_E$ and $10.7R_E$. In addition, the amplitude of the low frequency electromagnetic waves increases from $\delta B \sim 0.5B_0$ to $\sim 2.5B_0$ as the solar wind speed increases from $M_A = 3.0$ to 8.0.

Under the same direction of n, magnetosheath reconnection occurs more frequently inside the RD in case with a larger M_A. Figures 13a–13c show the magnetic field line configuration in cases with M_A=3.0 (Case 2, Figure 13a), 5.6 (Case 1, Figure 13b), and 8.0 (Case 3, Figure 13c). The contours display the B_z component in the noon meridian plane. The orange field lines denote the magnetic field lines around the RD. As shown in Figure 13a, in Case 2 with $M_A = 3.0$, no reconnection flux ropes are found inside the RD because the compression processes of the RD are weakened with a smaller $M_A = 3.0$. When M_A increases to 5.6, magnetosheath flux ropes with a length of $\sim 60d_{i0}$ are present in Case 1, as shown in Figure 13b. For Case 3, in which M_A is further increased to 8.0, a longer magnetosheath flux rope with a length of $\sim 100.d_{i0}$ is formed, but the reconnection rate is similar to that in Case 1. Moreover, reconnection is also not found downstream of the Q-∥ shock after the RD passes through the magnetopause. In the case with a larger M_A, the shock compression and convection compression processes become stronger, and a thinner current sheet is formed (especially on the duskside and dawnside). Thus, magnetic reconnection is more likely to take place, resulting in the generation of a longer flux rope in the dawn-dusk direction. In addition, the stronger low-frequency waves from the Q-∥ shock also play an important role in the triggering of the magnetosheath reconnection. Overall, longer magnetosheath flux ropes are found in the cases with a larger M_A.

3.3. Cases 4–5 With Various Propagation Direction n

To investigate the effects of the propagation direction n of the RD on the magnetosheath reconnection, where $n = (-\sin(\theta_{12}/2), 0, -\cos(\theta_{12}/2))$, Figures 14a and 14b show the magnetic field line configuration

B$_z$/B$_0$:
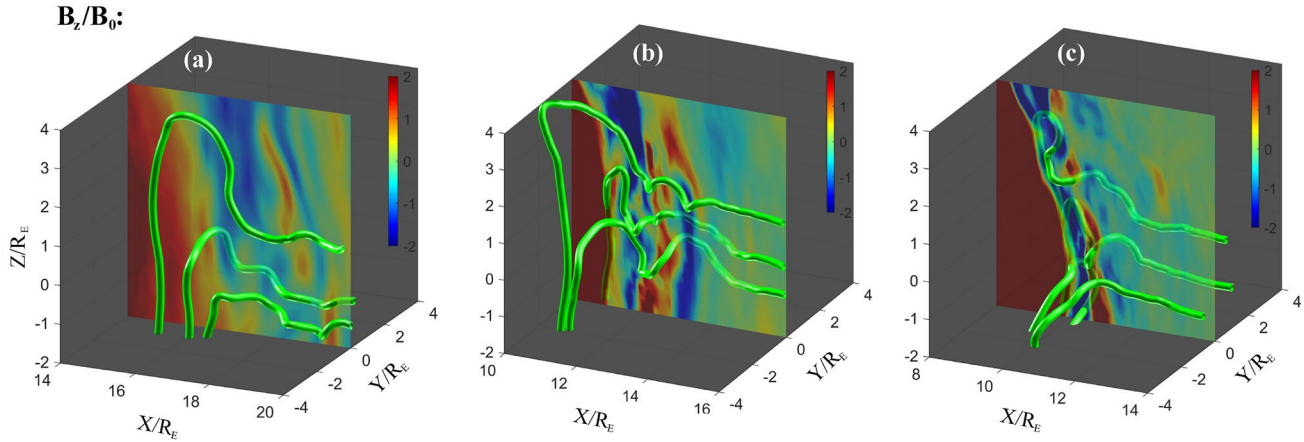
Figure 12. Magnetic field line configuration in a zoom-in view around the Q-∥ shock in cases with (a) $M_A = 3.0$ (Case 2), (b) $M_A = 5.6$ (Case 1), (c) $M_A = 8.0$ (Case 3), assuming $\theta_{12} = 90°$. The contours in the noon meridian plane display the B_z component. The green field lines mark the magnetic field lines around the Q-∥ shock.

downstream of the bow shock, for cases with $\theta_{12} = 135°$ (Case 4, Figure 14a), and 70° (Case 5, Figure 14b), assuming $M_A = 5.6$ and the initial IMF is purely northward. The contour plots in the figure show, again, the B_z component. The orange lines are the field lines inside the RD in the magnetosheath, the red field lines mark the flux ropes at the magnetopause, and the black field line represents the magnetic field line just inside the magnetopause. In Case 4 with $\theta_{12} = 135°$, the propagation direction of the RD is $n = (-0.9239,0,-0.3827)$. The magnetic field $(B_{2x},B_{2y},B_{2z}) = (0.7071,0,-0.7071)B_0$ behind the RD, and correspondingly the bow shock becomes the Q-∥ shock in $z < 0$ (shown in Figure 2b). Noted that no low-frequency waves are present in the region of the Q-⊥ shock ($z > 0$). In this case, magnetosheath flux ropes are not found until the RD moves very close to the magnetopause. For example, as shown in Figure 14a, reconnection flux rope (denoted by the orange field lines) with a length of ∼6d_{i0} is present inside the RD at $(x,z) = (9.8,2.7)R_E$ downstream of the Q-⊥ shock, at a distance very close to the magnetopause (∼0.3R_E), obtained at $t = 120\Omega_{i0}^{-1}$. In addition, the magnetopause flux ropes are present at $(x,z) = (9.1,4.2)R_E$ by the magnetopause reconnection, denoted by the red field lines in Figure 14a. Compared with Case 4, low-frequency waves are present in the region of $0 < z < 13.5R_E$ in Case 1 with $\theta_{12} = 90°$. The magnetosheath flux ropes are formed at $t \approx 80\Omega_{i0}^{-1}$ in Case 1, earlier than that in Case 4 ($t \approx 120\Omega_{i0}^{-1}$). Moreover, the reconnection flux ropes in Case 1 are found downstream of the Q-∥ shock, at a distance much farther from the magnetopause (∼1.6R_E) than that in Case 4 (∼0.3R_E)

B$_z$/B$_0$:
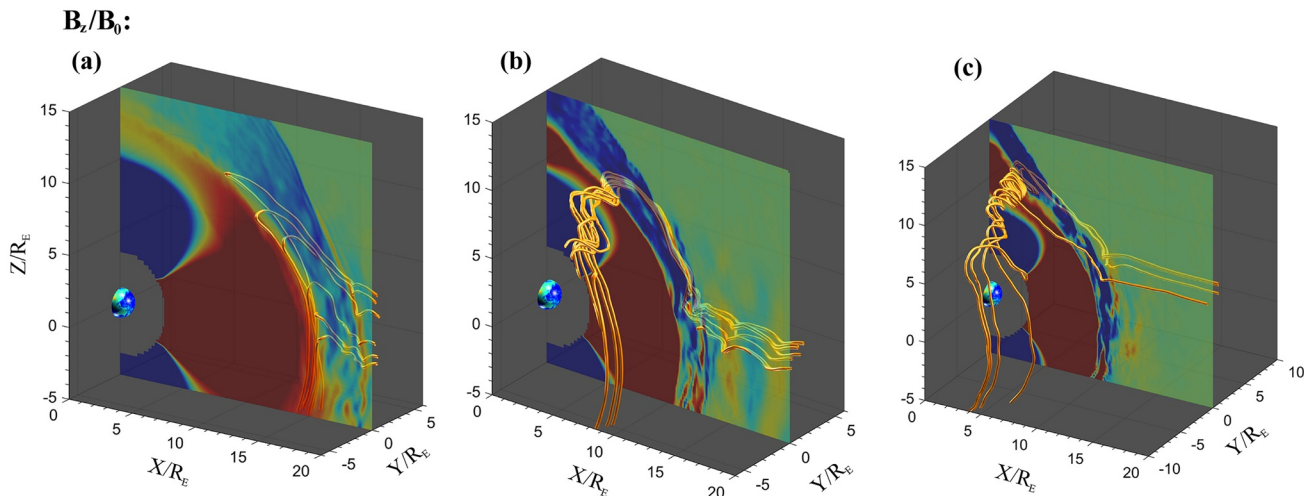
Figure 13. Magnetic field line configuration around the RD in cases with (a) $M_A = 3.0$ (Case 2), (b) $M_A = 5.6$ (Case 1), (c) $M_A = 8.0$ (Case 3), assuming $\theta_{12} = 90°$. The contours in the noon meridian plane show the B_z component. The orange field lines denote the field lines around the RD.
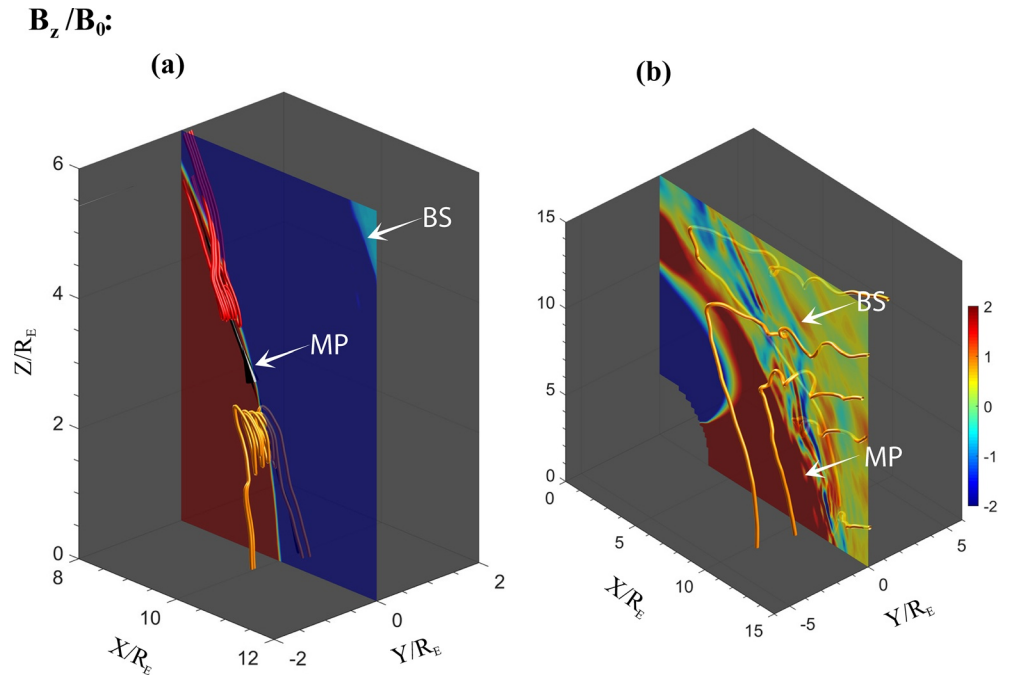
Figure 14. Contour plots of the B_z component in the noon meridian plane for cases with (a) $\theta_{12} = 135°$ (Case 4) and (b) $\theta_{12} = 70°$ (Case 5), assuming $M_A = 5.6$. The orange lines denote the magnetosheath field lines around the RD, the red ones mark the magnetopause flux rope, and the black line represents the magnetopause field lines. The bow shock location is denoted by "BS.".

downstream of the Q-⊥ shock. It indicates that the low frequency waves originated upstream of the Q-∥ shock play an important role in facilitating reconnection inside the RD in the magnetosheath.

In Case 5 with $\theta_{12} = 70°$, the propagation direction of the RD is $n = (−0.5736,0,−0.8192)$. The magnetic field $(B_{2x},B_{2y},B_{2z}) = (0.9397,0,0.3420)B_0$ behind the RD and the region of the Q-∥ shock is located at $z > −6.5R_E$ (Figure 2c). No reconnection is found in the magnetosheath, as shown in Figure 14b. We have also simulated cases with propagation direction n more oblique to the $−z$ axis ($\theta_{12} < 70°$), it is found that no magnetosheath flux ropes are present in the entire magnetosheath.

3.4. Cases 6 and 7 With Various Initial IMF Direction

To illustrate the effects of the initial shock structure on magnetosheath reconnection inside the RD, cases 6 and 7 with different initial IMF have been investigated. Compared with Case 1, the upstream field of the RD is assumed to be oblique, with $\mathbf{B_1} = (−0.7071,0,0.7071)B_0$ in Case 6 and $(0.3420,0,0.9397)B_0$ in Case 7. Behind the RD, the magnetic field $\mathbf{B_2} = (1.0,0,0)B_0$ and the solar wind Alfvén Mach number $M_A = 5.6$ in both cases, similar to that used in Case 1. The initial shock structure is Q-∥ in region of $z < 0$ for Case 6 and $z > −6.0R_E$ for Case 7, while the shock structure is almost Q-⊥ for Case 1 with a pure northward initial IMF. Figures 15a and 15b show the magnetic field line configuration inside the RD in a zoom-in view, obtained from Case 6 (Figure 15a) and Case 7 (Figure 15b) at $t = 100\Omega_{i0}^{-1}$. The contour plots in the noon meridian plane show the magnetic field strength B. The orange field lines represent the flux ropes in the magnetosheath, and the red lines are the field lines at the magnetopause. We find that reconnection flux ropes are present inside the RD in the magnetosheath at $(x,z) = (9.0,6.1)R_E$ in Case 6 and at $(x,z) = (8.8,6.4)$ R_E in Case 7. The reconnection rate in these two cases are also similar to that in Case 1. It indicates that the magnetosheath reconnection inside the RD still occurs when the initial shock structure is Q-∥. In addition, no reconnection is found downstream of the Q-∥ shock after the RD passes through the magnetopause.
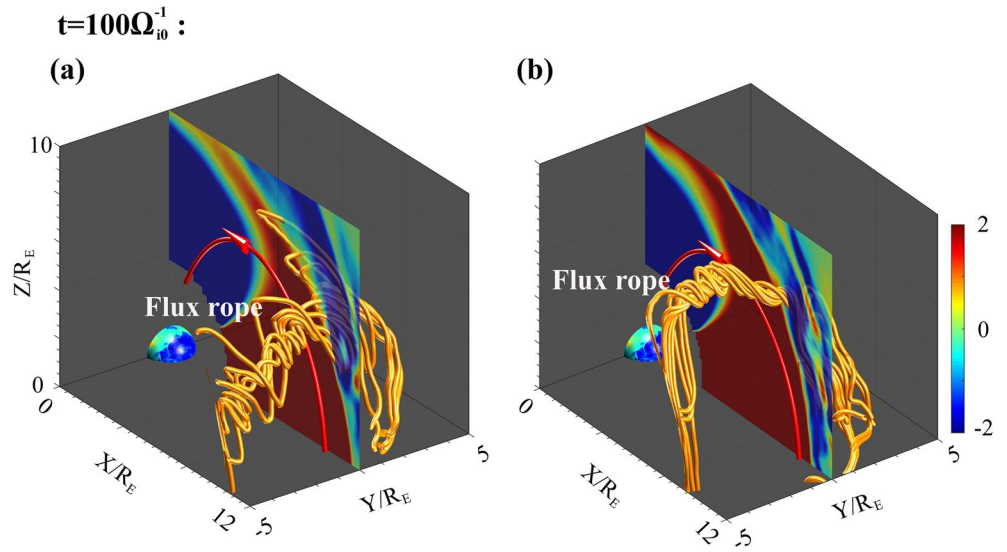
Figure 15. Magnetosheath field line configuration inside the RD in a zoom-in view obtained from (a) Case 6 and (b) Case 7 at $t = 100\Omega_{i0}^{-1}$. The contour plots in the noon meridian plane show the B_z component.

4. Summary and Discussion

In this study, we have used a 3D global hybrid simulation to study the interaction of the interplanetary RD with the bow shock, magnetosheath and magnetopause. Specifically, generation of reconnection downstream of the Q-∥ shock is investigated. The propagation direction of the RD is assumed to be earthward. Cases with various propagation directions n ($n = (-\sin(\theta_{12}/2), 0, -\cos(\theta_{12}/2))$) and solar wind Alfvén Mach numbers M_A have been investigated, where θ_{12} is the angle between the upstream (B_1) and downstream (B_2) magnetic fields of the RD. In addressing the questions raised in the introduction, we found no reconnection occurring in the turbulent bow shock and magnetosheath alone without the impact of RD, and the following main results are obtained regarding the generation of reconnection inside the RD.

1. Magnetosheath reconnection can be triggered inside the RD downstream of the Q-∥ shock by the shock/magnetosheath compression and the effects of the turbulent waves. The reconnection rate is ~0.08 around the X line inside the RD. The RD passes through the dayside magnetopause, new reconnection takes place between the field lines on the sunward side of the RD and geomagnetic field lines at the magnetopause. No magnetosheath reconnection is found downstream of the Q-∥ shock after the RD passes through the magnetopause. Our simulation shows that ion-scale magnetic reconnection is driven by the interaction of the interplanetary RD with the dayside bow shock/magnetosphere, rather than caused by the turbulent Q-∥ shock itself

2. The amplitude of low-frequency waves increases as M_A increases, which leads to more reconnection in the magnetosheath. For a fixed $\theta_{12} = 90°$ and a pure northward initial IMF, magnetosheath flux ropes are found in the magnetosheath with $M_A = 5.6$ and 8.0 downstream of the Q-∥ shock, while the length of the flux ropes in the case with $M_A = 8.0$ (~$100d_{i0}$) is longer than that in the case with the smaller $M_A = 5.6$ (~$60d_{i0}$), but the reconnection rate is similar to that in the case with $M_A = 5.6$. Nevertheless, in the case in which M_A decreases to 3.0, no magnetosheath flux ropes are present in the magnetosheath

3. The existence and structure of reconnection inside the RD are also strongly dependent on the propagation direction n of the RD. For a fixed $M_A = 5.6$ and purely northward initial IMF, the magnetosheath flux ropes are only present with a size of several d_{i0} in the case with $\theta_{12} = 135°$, at a distance very close to the magnetopause downstream of the Q-⊥ shock. When θ_{12} decreases to $\theta_{12} \leq 70°$, no magnetosheath flux ropes are found in the entire magnetosheath

4. Large-amplitude low-frequency waves are generated in the foreshock region, where the backstreaming reflected ion beam interacts with the incoming solar wind. The waves propagate nearly along the ambient field toward the Earth with a left-handed polarization in the simulation frame. As the waves penetrate into the magnetosheath, it can bend and squeeze the field lines around the RD, leading to the generation of a thin current sheet with a larger shear angle inside the RD, which in turn play an important role in facilitating magnetic reconnection inside the RD in the magnetosheath

Our simulations have shown that reconnection can take place downstream of the Q-∥ shock when an interplanetary RD is transmitted through the bow shock. As the RD is transmitted through the bow shock, it is compressed by the bow shock and then the magnetosheath. A thin current sheet with $B_n \sim 0$ is formed due to the existence of the differential flows in the magnetosheath and low-frequency waves downstream of the Q-∥ shock, leading to the generation of reconnection inside the RD. However, reconnection is found only in limited regions downstream of the Q-∥ shock. For example, in Case 4 with $\theta_{12} = 135°$, no reconnection flux ropes are present downstream of the Q-∥ shock in $z < 0$, because the southward magnetosheath flows drag the field lines in the way that they straighten the field lines across the RD. It indicates that the magnetosheath flows play an important role in the evolution of the RD downstream of the Q-∥ shock.

Our hybrid simulation does not include the physics on the electron kinetic scale. It has been widely believed that the electron dynamics is essential in the triggering processes of magnetic reconnection (e.g., Horiuchi & Sato, 1997; Ishizawa et al., 2004; Zenitani et al., 2011). By comparing the Hall-MHD simulations with the particle-in-cell (PIC) model, Hesse et al. (2001) identified that the overall evolution and growth of the reconnected magnetic flux behaved almost identically for the Hall-MHD and the PIC model. They concluded that the different dissipation processes may lead to similar large-scale behavior irrespective of the dissipation details, which is supported by hybrid simulations based on a simple fluid electron model (Kuznetsova et al., 2001). Compared with the Hall-MHD model, hybrid simulations contain the hot ion fully kinetic physics, in addition to the Hall effects. In our simulation, an ad hoc current-dependent resistivity is imposed to trigger magnetic reconnection. The model has been used to study the structure of magnetopause reconnection, and the results have been compared with MMS observations (e.g., Guo, Lin, Wang, Vines, et al., 2020). It was found that the spatial and temporal variations of the ion-scale reconnection layer, the electromagnetic power spectra, and the associated ion velocity distribution in the simulated reconnection event are well consistent with the observations. Nevertheless, fully kinetic simulations are necessary to reveal the electron kinetic physics of reconnection and, importantly, the occurrence of electron-only reconnection (e.g., Gingell, Schwartz, Eastwood, et al., 2019; Phan, Eastwood, et al., 2018; Yordanova et al., 2016).

Ion-scale reconnection has been observed in the magnetosheath (e.g., Polar: Maynard, Burke, et al., 2007; Cluster: Phan, Paschmann, et al., 2007; Retinò et al., 2007; THEMIS: Øieroset et al., 2017; Phan, Love, et al., 2011; MMS: Eastwood, Mistry, et al., 2018; Vörös et al., 2017), as well in the transition regions of the Q-⊥ bow shock (Hamrin et al., 2019). The observed reconnecting current sheets may be generated locally (e.g., Eastwood, Mistry, et al., 2018; Øieroset et al., 2017; Retinò et al., 2007; Vörös et al., 2017) or from the solar wind discontinuities (TDs or RDs) (e.g., Hamrin et al., 2019; Maynard, Burke, et al., 2007; Phan, Love, et al., 2011; Phan, Paschmann, et al., 2007). However, it might be challenging to determine where the reconnecting current sheet is originating from. Even though reconnecting current sheet is suggested to be caused by an external driver in the form of compression of an interplanetary directional discontinuity (DD) in the cases discussed by Phan, Paschmann, et al. (2007) and Hamrin et al. (2019), many questions still remain. For example, did reconnection already occur in the solar wind before the DD interacts with the bow shock? Is the DD compressed in the interactions, which then leads to the triggering of reconnection in the thin current sheet? What is the evolution on the global scale? Our hybrid simulation is adequate to study the ion-scale structures of reconnection. The global and local signatures of the electromagnetic field and plasma density and the parallel and perpendicular ion temperatures obtained from the simulation provide essential information for space observations of dayside reconnection.

In this article, we only focus on the large, ion-scale reconnection inside the RD. In our simulation, the RD is significantly slowed down when it reaches the bow shock. Ion-scale magnetic reconnection can be found inside the RD downstream of the Q-∥ shock while the RD is compressed around the bow shock and in the turbulent magnetosheath. After the RD leaves the tailward boundary, no ion-scale magnetosheath reconnection is seen in the turbulent sheath region. In addition, the simulated cases with different configurations

in the solar wind RD can help us better the processes of the interaction between the interplanetary current sheets (RDs) and bow shock/magnetosphere.

Data Availability Statement

The numerical data used for generating the presented figures are available via figshare (https://doi.org/10.6084/m9.figshare.13105808.v1).

References

Angelopoulos, V., McFadden, J. P., Larson, D., Carlson, C. W., Mende, S. B., Frey, H., et al. (2008). Tail reconnection triggering substorm onset. *Science*, *321*(5891), 931–935. https://doi.org/10.1126/science.1160495

Archer, M. O., Horbury, T. S., & Eastwood, J. P. (2012). Magnetosheath pressure pulses: Generation downstream of the bow shock from solar wind discontinuities. *Journal of Geophysical Research: Space Physics*, *117*(A5), A05228. https://doi.org/10.1029/2011ja017468

Behannon, K. W., Neubauer, F. M., & Barnstorf, H. (1981). Fine-scale characteristics of interplanetary sector boundaries. *Journal of Geophysical Research*, *86*(A5), 3273–3287. https://doi.org/10.1029/ja086ia05p03273

Bessho, N., Chen, L. J., Wang, S., Hesse, M., & Wilson, L. B., III (2019). Magnetic reconnection in a quasi-parallel shock: Two-dimensional local particle-in-cell simulation. *Geophysical Research Letters*, *46*(16), 9352–9361. https://doi.org/10.1029/2019gl083397

Birn, J., Drake, J. F., Shay, M. A., Rogers, B. N., Denton, R. E., Hesse, M., et al. (2001). Geospace Environmental Modeling (GEM) magnetic reconnection challenge. *Journal of Geophysical Research*, *106*(A3), 3715–3719. https://doi.org/10.1029/1999ja900449

Blanco-Cano, X., Omidi, N., & Russell, C. T. (2006). Macrostructure of collisionless bow shocks: 2. ULF waves in the foreshock and magnetosheath. *Journal of Geophysical Research*, *111*(A10), A10205. https://doi.org/10.1029/2005ja011421

Burlaga, L. F. (1969). Directional discontinuities in the interplanetary magnetic field. *Solar Physics*, *7*(1), 54–71. https://doi.org/10.1007/bf00148406

Cable, S., & Lin, Y. (1998). Three-dimensional MHD simulations of interplanetary rotational discontinuities impacting the Earth's bow shock and magnetosheath. *Journal of Geophysical Research*, *103*(A12), 29551–29568. https://doi.org/10.1029/1998ja900025

Cheng, L., Lin, Y., Perez, J. D., Johnson, J. R., & Wang, X. (2020). Kinetic Alfvén waves from magnetotail to the ionosphere in global hybrid simulation associated with fast flows. *Journal of Geophysical Research: Space Physics*, *125*(2), e2019JA027062. https://doi.org/10.1029/2019JA027062

Eastwood, J. P., Balogh, A., Lucek, E. A., Mazelle, C., & Dandouras, I. (2005). Quasi-monochromatic ULF foreshock waves as observed by the four-spacecraft Cluster mission: 1. Statistical properties. *Journal of Geophysical Research*, *110*(A11). https://doi.org/10.1029/2004JA010617

Eastwood, J. P., Mistry, R., Phan, T. D., Schwartz, S. J., Ergun, R. E., Drake, J. F., et al. (2018). Guide field reconnection: Exhaust structure and heating. *Geophysical Research Letters*, *45*(10), 4569–4577. https://doi.org/10.1029/2018gl077670

Gingell, I., Schwartz, S. J., Burgess, D., Johlander, A., Russell, C. T., Burch, J. L., et al. (2017). MMS observations and hybrid simulations of surface ripples at a marginally quasi-parallel shock. *Journal of Geophysical Research: Space Physics*, *122*(11), 11003–11017. https://doi.org/10.1002/2017ja024538

Gingell, I., Schwartz, S. J., Eastwood, J. P., Burch, J. L., Ergun, R. E., Fuselier, S., et al. (2019). Observations of magnetic reconnection in the transition region of quasi-parallel shocks. *Geophysical Research Letters*, *46*(3), 1177–1184. https://doi.org/10.1029/2018gl081804

Greene, J. M. (1992). Locating three-dimensional roots by a bisection method. *Journal of Computational Physics*, *98*(2), 194–198. https://doi.org/10.1016/0021-9991(92)90137-n

Guo, Z., Lin, Y., & Wang, X. (2021). Investigation of the interaction between magnetosheath reconnection and magnetopause reconnection driven by oblique interplanetary tangential discontinuity using three-dimensional global hybrid simulation. *Journal of Geophysical Research*, *126*(2), e2020JA028558. https://doi.org/10.1029/2020ja028558

Guo, Z., Lin, Y., Wang, X., & Du, A. (2018). Magnetosheath reconnection before magnetopause reconnection driven by interplanetary tangential discontinuity: A three-dimensional global hybrid simulation with oblique interplanetary magnetic field. *Journal of Geophysical Research: Space Physics*, *123*(11), 9169–9186. https://doi.org/10.1029/2018ja025679

Guo, Z., Lin, Y., Wang, X., Vines, S. K., Lee, S. H., & Chen, Y. (2020). Magnetopause reconnection as influenced by the dipole tilt under southward IMF conditions: Hybrid simulation and MMS observation. *Journal of Geophysical Research*, *125*(9), e2020JA027795. https://doi.org/10.1029/2020ja027795

Gutynska, O., Safrankova, J., & Nemeek, Z. (2009). Correlation properties of magnetosheath magnetic field fluctuations. *Journal of Geophysical Research*, *114*(A8), A08207. https://doi.org/10.1029/2009ja014173

Gutynska, O., Šimůnek, J., Šafránková, J., Němeček, Z., & Přech, L. (2012). Multipoint study of magnetosheath magnetic field fluctuations and their relation to the foreshock. *Journal of Geophysical Research*, *117*(A4), A04214. https://doi.org/10.1029/2011ja017240

Hamrin, M., Gunell, H., Goncharov, O., De Spiegeleer, A., Fuselier, S., Mukherjee, J., et al. (2019). Can reconnection be triggered as a solar wind directional discontinuity crosses the bow shock? A case of asymmetric reconnection. *Journal of Geophysical Research: Space Physics*, *124*(11), 8507–8523. https://doi.org/10.1029/2019JA027006

Hesse, M., Birn, J., & Kuznetsova, M. (2001). Collisionless magnetic reconnection: Electron processes and transport modeling. *Journal of Geophysical Research*, *106*(A3), 3721–3735. https://doi.org/10.1029/1999ja001002

Hoppe, M. M., & Russell, C. T. (1983). Plasma rest frame frequencies and polarizations of the low-frequency upstream waves: ISEE 1 and 2 observations. *Journal of Geophysical Research*, *88*(A3), 2021–2027. https://doi.org/10.1029/ja088ia03p02021

Horbury, T. S., Burgess, D., Fränz, M., & Owen, C. J. (2001). Three spacecraft observations of solar wind discontinuities. *Geophysical Research Letters*, *28*(4), 677–680. https://doi.org/10.1029/2000gl000121

Horiuchi, R., & Sato, T. (1997). Particle simulation study of collisionless driven reconnection in a sheared magnetic field. *Physics of Plasmas*, *4*(2), 277–289. https://doi.org/10.1063/1.872088

Ishizawa, A., Horiuchi, R., & Ohtani, H. (2004). Two-scale structure of the current layer controlled by meandering motion during steady-state collisionless driven reconnection. *Physics of Plasmas*, *11*(7), 3579–3585. https://doi.org/10.1063/1.1758718

Karimabadi, H., Roytershteyn, V., Vu, H. X., Omelchenko, Y. A., Scudder, J., Daughton, W., et al. (2014). The link between shocks, turbulence, and magnetic reconnection in collisionless plasmas. *Physics of Plasmas*, *21*(6), 062308. https://doi.org/10.1063/1.4882875

Karlsson, T., Plaschke, F., Hietala, H., Archer, M., Blanco-Cano, X., Kajdič, P., et al. (2018). Investigating the anatomy of magnetosheath jets - MMS observations. *Annales Geophysicae*, *36*(2), 655–677. https://doi.org/10.5194/angeo-36-655-2018

Kuznetsova, M. M., Hesse, M., & Winske, D. (2001). Collisionless reconnection supported by nongyrotropic pressure effects in hybrid and particle simulations. *Journal of Geophysical Research*, *106*(A3), 3799–3810. https://doi.org/10.1029/1999ja001003

Lee, G., & Russell, C. T. (1994). The morphology of ULF waves in the Earth's foreshock. In M. J. Engebretson, K. Takahashi, M. Scholer (Eds.), *Solar wind sources of magnetospheric ultra low frequency waves*. Geophysical Monograph Series (Vol. 81, pp. 87–98). AGU.

Lepping, R. P., & Behannon, K. W. (1986). Magnetic field directional discontinuities: Characteristics between 0.46 and 1.0 AU. *Journal of Geophysical Research*, *91*(A8), 8725–8741. https://doi.org/10.1029/ja091ia08p08725

Lin, Y. (1997). Generation of anomalous flows near the bow shock by its interaction with interplanetary discontinuities. *Journal of Geophysical Research*, *102*(A11), 24265–24281. https://doi.org/10.1029/97ja01989

Lin, Y., Lee, L. C., & Yan, M. (1996). Generation of dynamic pressure pulses downstream of the bow shock by variations in the interplanetary magnetic field orientation. *Journal of Geophysical Research*, *101*(A1), 479–493. https://doi.org/10.1029/95ja02985

Lin, Y., Swift, D. W., & Lee, L. C. (1996). Simulation of pressure pulses in the bow shock and magnetosheath driven by variations in interplanetary magnetic field direction. *Journal of Geophysical Research*, *101*(A12), 27251–27269. https://doi.org/10.1029/96ja02733

Lin, Y., & Wang, X. Y. (2005). Three-dimensional global hybrid simulation of dayside dynamics associated with the quasi-parallel bow shock. *Journal of Geophysical Research*, *110*(A12), A12216. https://doi.org/10.1029/2005ja011243

Lin, Y., Wang, X. Y., Lu, S., Perez, J. D., & Lu, Q. (2014). Investigation of storm time magnetotail and ion injection using three-dimensional global hybrid simulation. *Journal of Geophysical Research: Space Physics*, *119*(9), 7413–7432. https://doi.org/10.1002/2014ja020005

Liu, T. Z., Hietala, H., Angelopoulos, V., Omelchenko, Y., Roytershteyn, V., & Vainio, R. (2019). THEMIS observations of particle acceleration by a magnetosheath jet-driven bow wave. *Geophysical Research Letters*, *46*(14), 7929–7936. https://doi.org/10.1029/2019gl082614

Lu, Q., Wang, H., Wang, X., Lu, S., Wang, R., Gao, X., & Wang, S. (2020). Turbulence-driven magnetic reconnection in the magnetosheath downstream of a quasi-parallel shock: A three-dimensional global hybrid simulation. *Geophysical Research Letters*, *47*(1), e2019GL085661. https://doi.org/10.1029/2019GL085661

Maynard, N. C., Burke, W. J., Ober, D. M., Farrugia, C. J., Kucharek, H., Lester, M., et al. (2007). Interaction of the bow shock with a tangential discontinuity and solar wind density decrease: Observations of predicted fast mode waves and magnetosheath merging. *Journal of Geophysical Research*, *112*(A12), A12219. https://doi.org/10.1029/2007ja012293

Maynard, N. C., Sonnerup, B. U. Ö., Siscoe, G. L., Weimer, D. R., Siebert, K. D., Erickson, G. M., et al. (2002). Predictions of magnetosheath merging between IMF field lines of opposite polarity. *Journal of Geophysical Research*, *107*(A12), 1456. https://doi.org/10.1029/2002ja009289

Nagai, T., Fujimoto, M., Saito, Y., Machida, S., Terasawa, T., Nakamura, R., et al. (1998). Structure and dynamics of magnetic reconnection for substorm onsets with Geotail observations. *Journal of Geophysical Research*, *103*(A3), 4419–4440. https://doi.org/10.1029/97ja02190

Narita, Y., Glassmeier, K.-H., Schäfer, S., Motschmann, U., Fränz, M., Dandouras, I., et al. (2004). Alfvén waves in the foreshock propagating upstream in the plasma rest frame: Statistics from Cluster observations. *Annales Geophysicae*, *22*(7), 2315–2323. https://doi.org/10.5194/angeo-22-2315-2004

Øieroset, M., Phan, T. D., Shay, M. A., Haggerty, C. C., Fujimoto, M., Angelopoulos, V., et al. (2017). THEMIS multispacecraft observations of a reconnecting magnetosheath current sheet with symmetric boundary conditions and a large guide field. *Geophysical Research Letters*, *44*(15), 7598–7606. https://doi.org/10.1002/2017gl074196

Omidi, N., Phan, T., & Sibeck, D. G. (2009). Hybrid simulations of magnetic reconnection initiated in the magnetosheath. *Journal of Geophysical Research*, *114*(A2), A02222. https://doi.org/10.1029/2008ja013647

Pang, Y., Lin, Y., Deng, X. H., Wang, X. Y., & Tan, B. (2010). Three-dimensional hybrid simulation of magnetosheath reconnection under northward and southward interplanetary magnetic field. *Journal of Geophysical Research*, *115*(A3), A03203. https://doi.org/10.1029/2009ja014415

Phan, T. D., Eastwood, J. P., Shay, M. A., Drake, J. F., Sonnerup, B. U. Ö., Fujimoto, M., et al. (2018). Electron magnetic reconnection without ion coupling in Earth's turbulent magnetosheath. *Nature*, *557*(7704), 202–206. https://doi.org/10.1038/s41586-018-0091-5

Phan, T. D., Love, T. E., Gosling, J. T., Paschmann, G., Eastwood, J. P., Oieroset, M., et al. (2011). Triggering of magnetic reconnection in a magnetosheath current sheet due to compression against the magnetopause. *Geophysical Research Letters*, *38*(17), L17101. https://doi.org/10.1029/2011gl048586

Phan, T. D., Paschmann, G., Twitty, C., Mozer, F. S., Gosling, J. T., Eastwood, J. P., et al. (2007). Evidence for magnetic reconnection initiated in the magnetosheath. *Geophysical Research Letters*, *34*(14), L14104. https://doi.org/10.1029/2007gl030343

Pritchett, P. L. (2001). Geospace environment modeling magnetic reconnection challenge: Simulations with a full particle electromagnetic code. *Journal of Geophysical Research*, *106*(A3), 3783–3798. https://doi.org/10.1029/1999JA001006

Retinò, A., Sundkvist, D., Vaivads, A., Mozer, F., André, M., & Owen, C. J. (2007). In situ evidence of magnetic reconnection in turbulent plasma. *Nature Physics*, *3*(4), 235–238. https://doi.org/10.1038/nphys574

Russell, C. T., & Hoppe, M. M. (1983). Upstream waves and particles. *Space Science Reviews*, *34*, 155–172. https://doi.org/10.1007/978-94-009-7096-0_12

Scholer, M. (1990). Diffuse ions at a quasi-parallel collisionless shock: Simulations. *Geophysical Research Letters*, *17*(11), 1821–1824. https://doi.org/10.1029/gl017i011p01821

Shevyrev, N. N., Zastenker, G. N., Eiges, P. E., & Richardson, J. D. (2006). Low frequency waves observed by Interball-1 in foreshock and magnetosheath. *Advances in Space Research*, *37*(8), 1516–1521. https://doi.org/10.1016/j.asr.2005.07.072

Shi, F., Cheng, L., Lin, Y., & Wang, X. (2017). Foreshock wave interaction with the magnetopause: Signatures of mode conversion. *Journal of Geophysical Research: Space Physics*, *122*(7), 757–776. https://doi.org/10.1002/2016ja023114

Sibeck, D. G., Takahashi, K., Kokubun, S., Mukai, T., Ogilvie, K. W., & Szabo, A. (1997). A case study of oppositely propagating Alfvénic fluctuations in the solar wind and magnetosheath. *Geophysical Research Letters*, *24*(24), 3133–3136. https://doi.org/10.1029/97gl03263

Sonnerup, B. U. O., & Scheible, M. (1998). Minimum and maximum variance analysis. In G. Paschmann & P. W. Daly (Eds.), *Analysis methods for multi-spacecraft data* (ISSI Scientific Report, Chapter 1, pp. 185–220). ESA Publications Division.

Swift, D. W. (1996). Use of a hybrid code for global-scale plasma simulation. *Journal of Computational Physics*, *126*(1), 109–121. https://doi.org/10.1006/jcph.1996.0124

Tan, B., Lin, Y., Perez, J. D., & Wang, X. Y. (2011). Global-scale hybrid simulation of dayside magnetic reconnection under southward IMF: Structure and evolution of reconnection. *Journal of Geophysical Research*, *116*(A2), A02206. https://doi.org/10.1029/2010ja015580

Tsubouchi, K., & Matsumoto, H. (2005). Effect of upstream rotational field on the formation of magnetic depressions in a quasi-perpendicular shock downstream. *Journal of Geophysical Research*, *110*(A4), 04101. https://doi.org/10.1029/2004ja010818

Tsurutani, B. T., & Smith, E. J. (1979). Interplanetary discontinuities: Temporal variations and the radial gradient from 1 to 8.5 AU. *Journal of Geophysical Research*, *84*(A6), 2773–2787. https://doi.org/10.1029/ja084ia06p02773

Turc, L., Ganse, U., Pfau-Kempf, Y., Hoilijoki, S., Battarbee, M., Juusola, L., et al. (2018). Foreshock properties at typical and enhanced interplanetary magnetic field strengths: Results from hybrid-Vlasov simulations. *Journal of Geophysical Research: Space Physics*, *123*(7), 5476–5493. https://doi.org/10.1029/2018ja025466

Vörös, Z., Yordanova, E., Varsani, A., Genestreti, K. J., Khotyaintsev, Y. V., Li, W., et al. (2017). MMS observation of magnetic reconnection in the turbulent magnetosheath. *Journal of Geophysical Research: Space Physics*, *122*(11), 11442–11467. https://doi.org/10.1002/2017JA024535

Wang, H., Lin, Y., Wang, X., & Guo, Z. (2019). Generation of kinetic Alfvén waves in dayside magnetopause reconnection: A 3-D global scale hybrid simulation. *Physics of Plasmas*, *26*(7), 072102. https://doi.org/10.1063/1.5092561

Wang, R., Nakamura, R., Lu, Q., Baumjohann, W., Ergun, R. E., Burch, J. L., et al. (2017). Simultaneously observed ion- and electron-scale quadrants of the reconnection Hall magnetic field at magnetopause. *Physical Review Letters*, *118*(17), 175101. https://doi.org/10.1103/physrevlett.118.175101

Yan, M., & Lee, L. C. (1994). Generation of slow-mode waves in front of the dayside magnetopause. *Geophysical Research Letters*, *21*(7), 629–632. https://doi.org/10.1029/94gl00563

Yan, M., & Lee, L. C. (1996). Interaction of interplanetary shocks and rotational discontinuities with the Earth's bow shock. *Journal of Geophysical Research*, *101*(A3), 4835–4848. https://doi.org/10.1029/95ja02976

Yao, S. T., Shi, Q. Q., Guo, R. L., Yao, Z. H., Fu, H. S., Degeling, A. W., et al. (2020). Kinetic-scale Flux Rope in the Magnetosheath Boundary Layer. *The Astrophysical Journal*, *897*(2), 137. https://doi.org/10.3847/1538-4357/ab9620

Yordanova, E., Vörös, Z., Varsani, A., Graham, D. B., Norgren, C., Khotyaintsev, Y. V., et al. (2016). Electron scale structures and magnetic reconnection signatures in the turbulent magnetosheath. *Geophysical Research Letters*, *43*(12), 5969–5978. https://doi.org/10.1002/2016gl069191

Zenitani, S., Hesse, M., Klimas, A., & Kuznetsova, M. (2011). New measure of the dissipation region in collisionless magnetic reconnection. *Physical Review Letters*, *106*(19), 195003. https://doi.org/10.1103/physrevlett.106.195003